UC Santa Cruz

UC Santa Cruz Electronic Theses and Dissertations

Title

Minimum Energy Attitude Maneuvering of Cubesats with Reaction Wheels

Permalink

https://escholarship.org/uc/item/6zn7c61h

Author

Rivkin, Dmitriy

Publication Date

2016

Copyright Information

This work is made available under the terms of a Creative Commons Attribution License, availalbe at https://creativecommons.org/licenses/by/4.0/

Peer reviewed|Thesis/dissertation

eScholarship.org Powered by the California Digital Library
University of California

UNIVERSITY OF CALIFORNIA

SANTA CRUZ

Minimum Energy Attitude Maneuvering of Cubesats with Reaction Wheels

A thesis submitted in partial satisfaction
of the requirements for the degree of

MASTER OF SCIENCE

in

COMPUTER ENGINEERING
with an emphasis in ROBOTICS & CONTROL

by

Dmitriy Rivkin

June 2016

The Thesis of Dmitriy Rivkin
is approved:

_____

Professor Gabriel Elkaim, Chair

_____

Professor Qi Gong

_____

Professor Renwick Curry

_____

Tyrus Miller
Vice Provost and Dean of Graduate Studies

Copyright © by

Dmitriy Rivkin

2016

Table of Contents

List of Figures

List of Tables

Abstract

Minimum Energy Attitude Maneuvering of Cubesats with Reaction Wheels

by

Dmitriy Rivkin

Utilization of reaction wheel array attitude control systems aboard Cubesats is challenging because they tend to consume a significant fraction of the energy budget. In this thesis, battery energy losses incurred by large angle maneuvers in the absence of a regenerative braking system are optimized using a Legendre pseudospectral direct optimal control method. Numerical challenges arising from non-smoothness of the power model are overcome. The value of optimizing battery losses rather than the integral of the sum of squares of control torque is evaluated as a function of system and maneuver parameters. Improvements are found to be significant when the moments of inertia of the reaction wheels are small. Both approaches are shown to outperform the industry standard eigenaxis maneuver. A method for rapidly computing near optimal solutions in orbit based on interpolation from a bank of precomputed solutions is proposed. Optimal trajectories are executed on a real reaction wheel.

Acknowledgments

I would like thank Professor Ren Curry for helping me write, Professor Qi Gong for teaching me about optimal control, and my adviser, Professor Gabe Elkaim, for giving me the freedom and support to pursue my research interests. I would also like to thank all the members of the Autonomous Systems Lab for their help and their ideas. Finally, a special thank you to Natasha Dudek for her unwavering emotional support and endless enthusiasm for all things beyond the stratosphere.

1 Introduction

Cubesats are very small, very low-cost satellites about the size of a loaf of bread, that are affordable to a much broader user base than conventional (normal scale) satellites, including universities [15], start-ups [20], and even non-government space exploration societies[32]. They are comparable to modern smartphones in that they are both compact and inexpensive packages that provide access to technology previously too expensive for most to afford. In both cases the availability of technology in an affordable package allows for novel usage modalities. For example, the QB50 mission used a swarm of Cubesats making measurements upon atmospheric re-entry to study the upper atmosphere [15], a mission that would not have been economically feasible using full scale satellites. Unfortunately, the low pricetag is the result of extreme size, weight, and power (SWaP) constraints. The severity of these constraints motivates the optimization of spacecraft components.

One component that can take up a significant fraction of the SWaP budget is the attitude control system. Broadly speaking, the actuation torque a controller is capable of producing is proportional to its size. Light, compact actuators, such as magnetic torquers (electromagnetic coils which produce a control torque through interaction with the Earth's magnetic field), are capable of stabilizing the spacecraft against the small disturbance torques present in low Earth orbit, but cannot maneuver quickly or achieve high pointing accuracy. A class of higher performing, bulkier actuators includes includes cold gas thrusters, control moment gyros (CMG), and reaction wheel arrays (RWA). Cold gas thrusters consume fuel which needs to be stored and cannot be recovered. CMGs are mechanically complex, as they require an actuated gimble. Reaction wheel arrays are mechanically simple and do not consume any fuel, making them a popular attitude control method, especially for small satellites. However, all active attitude control systems require additional volume, power, complexity, and computation.

The intent of this work is to help RWA designers increase the efficiency of their

systems through trajectory optimization. The efficacy and value of this approach depend on the myriad specifics of the mission. However, there are relationships between certain key control system parameters, energy consumption, and the energy saving potential of trajectory optimization. This work explores these relationships to help designers develop an intuition for some ways in which they can reduce the energy consumption of their systems, and potentially the weight and volume as well. The solutions presented in this work are the results of analysis, simulation, and optimization of a hypothetical system with physical parameters similar to those of a 3 unit Cubesat (defined by the Cubesat standard [10]) with three reaction wheels. We believe that many of the trends identified and techniques used in this work are applicable to the design of larger spacecraft as well. To obtain maximum benefit, designers should adapt the analysis to reflect the specifics of their systems.

1.1 Reaction Wheel Array Attitude Controller

The RWA is a momentum exchange device. A momentum wheel is attached to the rotor of an electric motor, the stator of which is coupled to the body of the satellite. When the motor applies a torque to the reaction wheel, an equal and opposite torque is exerted on the satellite body, producing an angular acceleration. A minimum of three reaction wheels allow for full control in three axes. RWAs with three wheels are normally arranged orthogonally. On larger satellites, the RWA often consists of a tetrahedral array of four reaction wheels; this arrangement is robust to failure of any one of the reaction wheels. However, due to severe volume and weight constraints, short orbital lifespans, and the relatively low cost of replacing a malfunctioning satellite, Cubesat RWAs usually only have three wheels. Because all torque is produced only by electric motors, RWA attitude control consumes only electrical energy, which is generated by solar panels covering the satellite body.

RWAs do not produce external torques, i.e. the angular momentum of the satellite body / RWA system remains constant even as the wheels and satellite accelerate in opposite directions by the law of conservation of angular momentum. In order to

keep the satellite stable in the presence of external torque, the RWA must accelerate, absorbing the extra momentum. If no action is taken to dump this extra momentum, the RWA will eventually saturate, and will no longer be able to exert the necessary control torques on the body. To avoid saturation, the RWA must be coupled with a controller that is capable of producing a torque against the external environment, in order to dump the momentum. Usually this secondary controller is based on magnetic torquers. While not capable of performing fast maneuvers on their own, the electromagnetic torquers can produce enough torque to compensate for external disturbances (e.g. atmospheric drag, solar wind, and gravity gradient torque).

For detailed background discussion of RWAs, see [36].

1.1.1 Momentum Wheels

It is desirable for momentum wheels to have a large Moment of Inertia (MOI) about their rotational axes. The higher the MOI of the wheels, the higher the maximum body angular rate the RWA can produce, and the more external torque the system can absorb before saturation occurs. Another advantage of high reaction wheel MOI stems from the fact that Cubesats are often deployed with a non-zero angular body rate, a scenario known as tumbling. Reaction wheels of sufficient MOI can detumble a satellite by absorbing the angular momentum of the spacecraft. All of these advantages stem from the fact that wheels with higher MOI can absorb more angular momentum before saturating. Higher-MOI reaction wheels also require lower energy consumption during large angle attitude maneuvers, as will be shown in Chapter 5.

The moment of inertia of a disk about its rotational axis can be computed as follows:

$$MOI = \frac{1}{2}mr^2 \tag{1}$$

where m and r are the mass and radius of the disk. Examination of Eq. 1 reveals the cost of high-MOI reaction wheels: higher MOI either requires more mass or a larger radius. Increasing the radius makes the wheel less compact, resulting in a greater

system volume. Increasing mass is also undesirable, due to the strict weight budget. Because reaction wheels with higher MOI tend to be heavier and more voluminous, they are sometimes referred to simply as "larger" reaction wheels in the remainder of this document. As demonstrated in this work, a RWA should have the smallest wheels that meet performance specifications and energy consumption limits.

1.1.2 Motors and Motor Drivers

Brushless DC (BLDC) motors, sometimes also known as permanent magnet synchronous motors (PMSM), are used to drive the reaction wheels. Compared to DC motors, BLDCs are more efficient and do not produce carbon dust, which is especially beneficial in a weightless, electronics-dense environment. Unlike DC motors, which are mechanically commutated by carbon brushes, BLDCs are electronically commutated; the user must control the stator current to produce the desired torque. This control is achieved using switch-mode electronics and a micro-controller. For more on BLDC motors and control, refer to [24]. If the stator currents of the motor's three phases, as well as the position of the rotor, can be accurately measured, a sophisticated motor control algorithm can precisely produce the desired control torque. Cubesat motor drivers are often less sophisticated, and are better suited to speed control than torque control. Cubesats motor drivers are also often incapable of regenerative braking, a mode of operation in which kinetic rotational energy of the reaction wheel is converted back into stored battery energy, as adding regenerative braking capabilities increases the complexity of the satellite's power system.

1.2 Eigenaxis Maneuvers

A convenient and popular method of computing trajectories for large angle attitude maneuvers is to constrain the satellite to rotation about a single axis called the eigenaxis [38]. The eigenaxis maneuver takes the shortest kinematic path between two attitudes. An angular body rate profile is then chosen to ensure that the satellite

reaches the desired attitude within the required time. The shape of this profile has a significant effect on the energy consumption of the maneuver. In order to evaluate the improvements in energy consumption afforded by trajectory optimization, the eigenaxis maneuver is used as a baseline. The angular velocity profile is chosen such that the velocity increases at a constant rate until the midpoint, and then decreases at the same rate until the endpoint, so that the satellite comes to rest at the desired attitude. Optimization of the velocity profile is beyond the scope of this work, but the constant acceleration approach produces energy consumption that is on the same order of magnitude as that of the energy optimal maneuvers, in contrast with the energy consumed by time optimal maneuvers, which are about 50-100 times more energetically costly.

1.3 Related Work

1.3.1 Trajectory Optimization

Trajectory optimization is concerned with the computation of a state/control trajectory pair that minimizes some cost metric. The cost metric in this type of optimization depends on variables which are themselves functions of time, thus the cost metric is referred to as a cost *functional*; a function of functions. With the exception of [22], the following works optimize a cost functional which depends only on control torque. Some authors refer to this kind of optimization as energy optimal, while other use the term "torque optimal", which is more accurate. [12] computed trajectories that minimized the integral of the sum of squares of control torques for an attitude controller with cold gas thrusters and magnetic torquers. [19] minimized the integral of control torque magnitude, without modeling the actuator producing the torque, while accounting for external disturbances. [21] modeled the dynamics of the reaction wheel array, and computed optimal trajectories in the presence of path constraints, minimizing a cost functional that included terms accounting for both maneuver time and control torque magnitude. [22] optimized a model-based

cost functional which more accurately modeled the energy losses of the RWA, and demonstrated that the energy cost of the optimal maneuver is inversely proportional to maneuver time by constructing a Pareto-optimal curve of maneuver time versus energy consumption. This is the only discussion of the effect of optimization parameters on the minimum energy trajectory that we are aware of. [22] also computed time-optimal maneuvers with energy constraints, as well as energy optimal eigenaxis trajectories. Other works tend to focus on obtaining solutions to a single, specific problem. Bedrossian's large angle maneuver of the international space station using only CMGs is the best known example of spacecraft attitude trajectory optimization [6]. It is dissimilar from the other work mentioned above in that its main objective was to avoid saturation of the CMGs due to external torques during a maneuver. Saturation of Cubesat RWAs occurs on a significantly longer time scale than that of a single maneuver, and can be compensated for with magnetic torquers. Apart from [19], these works focus on satellites much larger than Cubesats.

All of the work above applied pseudospectral optimal control methods to compute trajectories numerically. The same methods are also often applied to compute time optimal trajectories as well. In fact, there is a large volume of work on minimum time trajectory optimization of satellite attitude maneuvers [31],[8],[23],[14],[13]. Since there exists a trade-off between time and energy in the satellite reorientation problem [22], time-optimal maneuvers tend to be energetically expensive. Notably, however, the time optimal work of [18] illustrates a way in which optimal attitude maneuvers for RWAs computed using pseudospectral optimal control methods can be implemented in practice. Maneuvers are computed on the ground and uploaded to an imaging satellite. The quaternion attitude trajectories are tracked using a proportional feedback control law. A significant improvement over eigenaxis trajectories was demonstrated.

1.3.2 Torque Allocation

The torque allocation problem arises when the RWA has more than three wheels. In this case, there are an infinite number of combinations of individual reaction wheel torques that produce the desired net control torque on the satellite body, and the problem is choosing the combination that minimizes energy consumption. The desired control can be computed via trajectory optimization, or by a feedback controller tracking an eigenaxis trajectory. Examples of such work include [9],[39], and [30]. The torque allocation problem is not closely related to the trajectory optimization problem, but is mentioned here because solutions to the torque allocation problem are sometimes referred to as energy optimal or power optimal.

1.4 Contributions

The following is an enumeration of work presented in this thesis:

1. The model based cost functional in [22] is adapted to model the non-regenerative braking case, and resulting numerical challenges are overcome using approximation and problem reformulation. The benefits of optimization with respect to this complex cost functional rather than a simpler, more convenient cost are evaluated extensively.

2. An efficient method for computation of near optimal solutions is proposed. This method is based on linear interpolation of precomputed solutions.

3. Relationships between parameter values, energy costs, and the utility of trajectory optimization are explored. The parameters investigated include reaction wheel MOI, final attitude, and maneuver time. Understanding of these relationships may aid Cubesat designers in making appropriate tradeoffs.

2 Energy Optimal Trajectories

Trajectory optimization is achieved through the formulation and subsequent solution of an optimal control problem. First, relevant system parameters are identified and defined. Next, the constraints and cost metric are expressed in the standard optimal control problem form. Once so formalized, the problem is solved with a direct numerical method known as the Legendre pseudospectral method, which is briefly discussed. Finally, this chapter concludes with a discussion of some the numerical challenges that arise in using this method, and how they are overcome.

2.1 System Definition

The system modeled in this work is a 3 unit Cubesat with three reaction wheels whose axes of rotation are parallel to the axes of the body reference frame. Its dimensions are $10cm \times 10cm \times 30cm$, and its mass is $3kg$. The origin of the body frame is at the satellite's center of mass. The body reference frame axes are perpendicular to the satellite's faces, as shown in Figure 1. The x, y, and z axes are also referred to as 1, 2, and 3, respectively. A particular reaction wheel is referred to by the axis parallel to its axis of rotation.

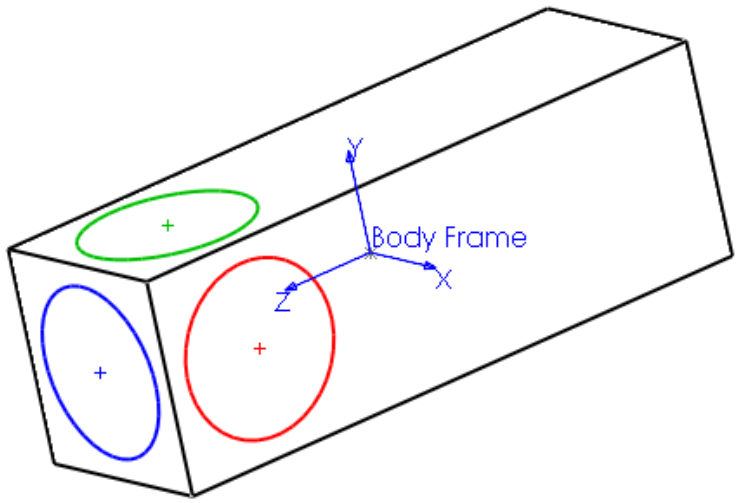

Figure 1: Sketch of satellite body frame and reaction wheel orientations.

Unless otherwise specified:

$$\boldsymbol{I} = \begin{bmatrix} 248 & 0.21 & 0.61 \\ 0.21 & 248 & 0.61 \\ 0.61 & 0.61 & 49 \end{bmatrix} \times 10^{-4}\ kg \cdot m^2 \tag{2}$$

$$I_w = 2.2 \times 10^{-5}\ kg \cdot m^2 \tag{3}$$

where $\boldsymbol{I}$ is the MOI tensor of the satellite body and I_w is the MOI of the reaction wheels about their axes of rotation. Unless otherwise specified, all three reaction wheels have the same MOI. The BLDC motors are 12 volt Faulhaber 2610s [3] with the following parameters:

$$R_a = 28.2\ \Omega \tag{4}$$

$$k_t = 1.81 \times 10^{-2}\ N \cdot m/A \tag{5}$$

$$\mu = 1.29 \times 10^{-7}\ N \cdot m/(rad/s) \tag{6}$$

where R_a is the armature resistance, k_t is the motor torque constant, and μ is the rotor dynamic friction coefficient. Since the wheels operate in the vacuum of space, the only source of friction is the motor bearings. The value of k_e, the motor electrical constant, is equal to k_t when both are expressed in S.I. units.

The maximum speed of the motors is 650 rad/s. The maximum torque production is dependent on the motor speed. However, a constant torque limit of $3.0 \times 10^{-3}\ N \cdot m$ is used in optimization and simulation since this level of torque production is achievable at all speeds. In practice, for most problems, the magnitude of energy optimal control torque trajectories stays well below the limits, since effecting large torques consumes large quantities of energy. Saturation only occurs when the time allotted for a maneuver is close to the minimum feasible time (see Chapter 5).

2.2 Optimal Control Problem Formulation

To enable formulation as an optimal control problem, relevant physical quantities must be cast as state and control variables. Notation is adopted from [29], where a boldface font indicates a column vector.

$\boldsymbol{x}$ is the state vector, containing all quantities with dynamic constraints. $\boldsymbol{u}$ is the control vector, containing quantities with algebraic constraints only. All quantities contained in $\boldsymbol{x}$ and $\boldsymbol{u}$ are time varying, but (t) notation is dropped for compactness, except when it is necessary to specify a value of $\boldsymbol{x}$ or $\boldsymbol{u}$ at some exact instant.

The vector $\boldsymbol{u}$ is comprised of the three reaction wheel motor torques ($\boldsymbol{u} = [\tau_1 \ \tau_2 \ \tau_3]^T$). The vector $\boldsymbol{x}$ contains the angular rate of the satellite body frame relative to the inertial frame ($\boldsymbol{\omega} = [\omega_x \ \omega_y \ \omega_z]^T$), the angular rates of the three reaction wheels about their spin axes with respect to the satellite body frame ($\boldsymbol{\omega_w} = [\omega_{w,1} \ \omega_{w,2} \ \omega_{w,3}]^T$), and the unit quaternion expressing the orientation of the body frame relative to the inertial frame ($\boldsymbol{q} = [q_0 \ q_1 \ q_2 \ q_3]^T$). In summary, $\boldsymbol{x} = [\boldsymbol{\omega}^T \ \boldsymbol{\omega_w}^T \ \boldsymbol{q}^T]^T$.

Any attitude can be represented as a rotation by a certain angle around a single axis. The unit quaternion is a vector with four entries, containing information about the axis and and the angle of rotation. The unit attitude quaternion definition is given by Eq. 7, where $\boldsymbol{e} = [e_x \ e_y \ e_z]^T$ is the unit vector expressing the axis of rotation, and θ is the angle of rotation.

$$\boldsymbol{q} = \begin{bmatrix} cos(\frac{\theta}{2}) \\ e_x sin(\frac{\theta}{2}) \\ e_y sin(\frac{\theta}{2}) \\ e_z sin(\frac{\theta}{2}) \end{bmatrix} \tag{7}$$

The magnitude of a quaternion is given by Eq. 8. The unit attitude quaternion has

a magnitude of 1.

$$||\boldsymbol{q}|| = \sqrt{\boldsymbol{q}^T\boldsymbol{q}} \tag{8}$$

With the states and controls defined, the optimal control problem is formulated as follows:

$$\text{Minimize cost functional} \quad J = \int_{t_0}^{t_f} g(\boldsymbol{x}, \boldsymbol{u})\, dt \tag{9}$$

$$\text{Subject to :} \quad \dot{\boldsymbol{x}} = \boldsymbol{f}(\boldsymbol{x}, \boldsymbol{u}) \tag{10}$$

$$\boldsymbol{x}(t_0) = \mathbf{x_0} \tag{11}$$

$$\boldsymbol{x}(t_f) = \mathbf{x_f} \tag{12}$$

$$\mathbf{u_L} \leq \boldsymbol{u} \leq \mathbf{u_U} \tag{13}$$

$$\mathbf{x_L} \leq \boldsymbol{x} \leq \mathbf{x_U} \tag{14}$$

$$t_0 \text{ and } t_f \text{ fixed} \tag{15}$$

$$\|\boldsymbol{q}\| = 1 \tag{16}$$

2.2.1 Constraints

Equations 10 - 16 specify constraints that must be satisfied by the solution. If no solution can be found that satisfies all the constraints, the problem is called infeasible. Eq. 10 requires that the solution respects the dynamics of satellite, described by the set of first order differential equations given below. Eq. 11 initializes the state vector. For all the solutions in this document, the body rate and reaction wheel speeds are all initialized at 0, and $\boldsymbol{q}(t_0) = [1\ 0\ 0\ 0]^T$. Eq. 12 constrains the final state, where $\boldsymbol{\omega}(t_f) = [0\ 0\ 0]^T$, and $\boldsymbol{q}(t_f)$ specifies the required final attitude. The final reaction wheel rates are not constrained, but because there are only three reaction wheels and disturbance torques are neglected, the reaction wheels are effectively constrained to be stationary at t_f by the dynamics. Eq. 13 is the algebraic constraint on control, and enforces motor torque limits. Eq. 14 is the algebraic state

constraint, wherein the maximum reaction wheel speed is limited to the maximum speed supported by the motors. Eq. 14 does not constrain $\boldsymbol{\omega}$ and $\boldsymbol{q}$. Eq. 15 fixes the initial and final times. By convention, $t_0 = 0$. Unless it is otherwise specified, $t_f = 30s$ for the solutions presented in this document. Finally, Eq. 16 is a path constraint, requiring that that $\boldsymbol{q}$ remains a unit quaternion at all times.

The spacecraft dynamics, $\boldsymbol{f}(\boldsymbol{x}, \boldsymbol{u})$, are derived in [18] and given below:

$$\begin{bmatrix} \dot{\boldsymbol{\omega}} \\ \dot{\boldsymbol{\omega}_w} \end{bmatrix} = \boldsymbol{\Gamma}^{-1} \begin{bmatrix} -\boldsymbol{\omega} \times (\boldsymbol{I}\boldsymbol{\omega} + \sum_{i=1}^{3} \boldsymbol{a}_i I_{w,i} \boldsymbol{\omega}_{w,i} + \boldsymbol{a}_i I_{w,i} \boldsymbol{a}_i^T \boldsymbol{\omega}) \\ \boldsymbol{u} \end{bmatrix}$$

$$\boldsymbol{\Gamma} = \begin{bmatrix} \boldsymbol{I} + \sum_{i=1}^{3} \boldsymbol{a}_i I_{w,i} \boldsymbol{a}_i^T & \boldsymbol{a}_1 I_{w,1} & \boldsymbol{a}_2 I_{w,2} & \boldsymbol{a}_3 I_{w,3} \\ I_{w,1} \boldsymbol{a}_1^T & I_{w,1} & 0 & 0 \\ I_{w,2} \boldsymbol{a}_2^T & 0 & I_{w,2} & 0 \\ I_{w,3} \boldsymbol{a}_3^T & 0 & 0 & I_{w,3} \end{bmatrix}$$

$$\dot{\boldsymbol{q}} = \frac{1}{2} \boldsymbol{q} \otimes \begin{bmatrix} 0 \\ \boldsymbol{\omega} \end{bmatrix}$$

where $\boldsymbol{I}$ is the MOI tensor of the spacecraft body, and $I_{w,i}$ is the MOI of reaction wheel i about its axis of rotation. The vector $\boldsymbol{a}_i$ expresses the orientation of the axis of rotation of reaction wheel i with respect to the body frame. $\otimes$ is the quaternion multiplication operator.

2.3 Running Cost

While J in Eq. 9 is known as the cost functional, $g(\boldsymbol{x}, \boldsymbol{u})$ is called the running cost. In contrast with time minimization, where the choice of cost functional is obvious, the running cost in energy minimization should ideally reflect the power consumption of the system, the time integral of which is energy. Power consumption is highly system dependent, and may be challenging to model. A running cost based on a high fidelity power model may also not be well suited to optimization, and produce

significant numerical challenges. Therefore, a convenient approximation for power consumption is the sum of squares of control torque, $\boldsymbol{u}^T\boldsymbol{u}$, referred to as the torque running cost (TRC) in the remainder if this document. This quadratic running cost is smooth (infinitely differentiable over its whole domain) and convex, making it very well suited to numerical optimization. It also requires no modeling of loss sources. However, trajectories which are optimal with respect to this convenient running cost do not minimize energy consumption. This motivates the formulation of a power model based running cost.

2.4 Power Model

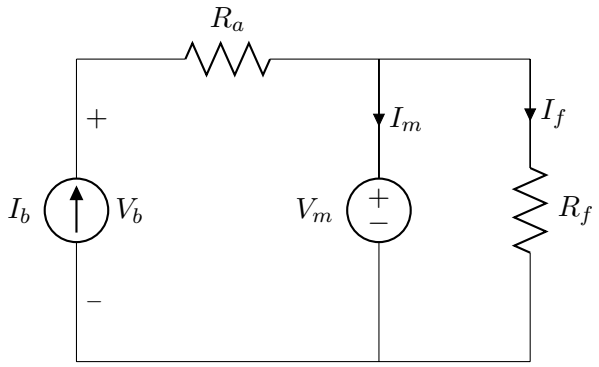

Figure 2: Circuit diagram of battery, drive electronics, and motor.

The following modeling and analysis, up to Eq. 23, are similar to those presented in [22]. The battery, drive electronics, and motor of a single reaction wheel are modeled by the circuit diagram in Figure 2. It is assumed that the drive electronics will supply the correct amount of current to produce the commanded motor torque, thus the battery and drive electronics are modeled by a current source with current I_b and voltage V_b. R_a is the armature resistance of the motor. V_m is the back electromotive force (EMF) produced by the rotation of the motor. The back EMF is linearly proportional to the wheel speed, ω_w, through the motor's electrical constant, k_e. I_m is the torque producing current, linearly proportional to the control torque, u, through the motor's torque constant, k_t. R_f models the power dissipation due to dynamic friction. I_f is the current required to compensate for dynamic friction

torque. Using this model, the power supplied by the battery (P_b) can be solved for as follows:

$$P_b = V_b I_b \tag{17}$$

$$V_b = V_m + I_b R_a \tag{18}$$

$$I_b = I_m + I_f \tag{19}$$

$$I_f = \frac{V_m}{R_f} \tag{20}$$

Combining Eq. 17 through Eq. 20:

$$P_b = V_m \left(I_m + \frac{V_m}{R_f} \right) + R_a \left(I_m + \frac{V_m}{R_f} \right)^2 \tag{21}$$

Recognizing that $V_m = k_e \omega_w$ and $I_m = u/k_t$, and rearranging:

$$P_b = u^2 \left(\frac{R_a}{k_t^2} \right) + u\omega_w \left(\frac{2R_a k_e}{k_t R_f} + \frac{k_e}{k_t} \right) + \omega_w^2 \left(\frac{k_e^2}{R_f} + \frac{k_e^2 R_a}{R_f^2} \right) \tag{22}$$

Finally, setting $R_f = k_e^2/\mu_f$, where μ_f is the motor's dynamic friction coefficient, ensures that R_f dissipates the appropriate amount of power ($\omega_w^2 \mu_f$), and the final result is obtained:

$$P_b = u^2 \left(\frac{R_a}{k_t^2} \right) + u\omega_w \left(\frac{2R_a \mu_f}{k_e k_t} + \frac{k_e}{k_t} \right) + \omega_w^2 \left(\mu_f + \frac{R_a \mu_f^2}{k_e^2} \right) \tag{23}$$

P_b has 3 terms. The first is the power dissipated by the armature resistance when torque-producing current flows through it. The last term is the power dissipated by dynamic friction, plus part of the power dissipated by the armature resistance due to the extra current needed to counteract the frictional force. The second term accounts for the mechanical power produced by the motor, plus the other part of the power dissipated by the armature resistance due to the extra current required to overcome the frictional force. While the first and third terms are always positive, the middle term is positive when the wheel is speeding up, and negative when it is slowing down. Therefore, when the motor is slowing down, it is possible for the

power to be negative, a mode of operation known as regenerative braking. This occurs when the deceleration demanded of the motor is less than it would be if the battery were removed and the terminals shorted together.

Eq. 23 models battery power losses of a system capable of perfect bidirectional power flow (regenerative braking). However, many Cubesats are not equipped with a power system capable of handling reverse power flow, and this power is dissipated as heat. Eq. 24 models the nonregenerative braking case.

$$P_b^+ = \begin{cases} P_b, & \text{if } P_b > 0 \\ 0, & \text{otherwise} \end{cases} \tag{24}$$

The model based running cost, hereafter referred to as the power running cost (PRC), for the nonregenrative braking case is obtained by adding the power consumption of all three reaction wheels:

$$PRC = \sum_{i=1}^{3} P_{b,i}^+ \tag{25}$$

In the rest of this work, all quantification of energy consumption is implemented by numerically integrating Eq. 25 from t_0 to t_f.

2.5 Solving the Optimal Control Problem

A Legendre pseudospectral method is used to solve the optimal control problem [27]. The pseudospectral approach is a direct method, meaning that the continuous time problem is discretized and solved numerically as a parameter optimization problem. In contrast, indirect methods apply Pontryagin's principle to the problem to produce a set of differential equations, the solution of which yields the optimal solution to the original problem [29]. Unlike other direct methods, which make local discretizations, pseudospectral methods approximate the trajectory of a variable with a single polynomial. Constraints are enforced at collocation points; discrete instances in

time at which the constraints are evaluated. A Legendre pseudospectral method uses the Legendre polynomials [37] as a basis for construction of the approximating polynomial. The collocation points are arranged in a Legendre-Gauss-Lobatto grid [16]. For a review of pseudospectral optimal control, see [28].

PSOPT is an open source optimal control package that uses a Legendre pseudospectral method to convert the problem into a nonlinear programming (NLP) problem [5], which is then solved by the NLP solver IPOPT (Interior Point OPTimizer) [34]. IPOPT, in turn, uses one of a number of available linear solvers to obtain a solution. PSOPT is a fast solver because it uses the ADOL-C (Automatic Differentiation by OverLoading in C++) library [35] in order to compute requisite Jacobian and Hessian matrices automatically, in contrast with numerical perturbation methods.

The solutions produced by PSOPT consist of the values of the state and control variables at the collocation points. Methods that allow the use of these trajectories to improve the maneuvering of a real satellite are discussed in the following chapter.

2.6 Numerical Challenges

Numerical optimal control solvers are sensitive to a number of optimization parameters and properties of the cost functional. Improper choice of these parameters, or a poor problem formulation, results in divergence, or slow convergence, of the optimization algorithm. Just obtaining a feasible solution may require a fair amount of tuning. This work is concerned with the computation of large numbers of solutions to varying problems, so it is critical to establish a robust computational approach which will produce solutions under variable conditions.

2.6.1 Non-Smoothness of PRC

Attempting to solve the problem with the running cost given in Eq. 25 fails to produce a solution. This is because most nonlinear programming (NLP) methods

assume that the running cost is continuously differentiable with respect to states and controls. A cost functional with a running cost which violates this assumption often results in divergence or slow convergence of the solution [7]. The discontinuity of the derivative of the PRC cost at zero produces unwanted behavior. A smoothing approximation of the running cost can be used to obtain an approximate solution:

$$\hat{P_b^+} = \frac{1}{2}(\sqrt{P_b^2 + \alpha} + P_b) \,, \qquad \alpha > 0 \tag{26}$$

As the approximation parameter, α, approaches 0, $\hat{P_b^+}$ approaches P_b^+, as illustrated by Figure 3. Choosing a high value results in a running cost that is very well suited to optimization, but not very closely representative of the physical truth, while a low value produces an accurate running cost that shares the numerical difficulties of the original. Therefore, α should be chosen to be the smallest value that produces a solution. To obtain the best results, a homotopic approach can be applied, where a solution is computed for a certain value of α, and then that solution is used as the initial guess in the next iteration, with a lower α value. Compared to a cold start, where the initial guess is far from the optimal, this method decreases the minimum α value that yields a solution.

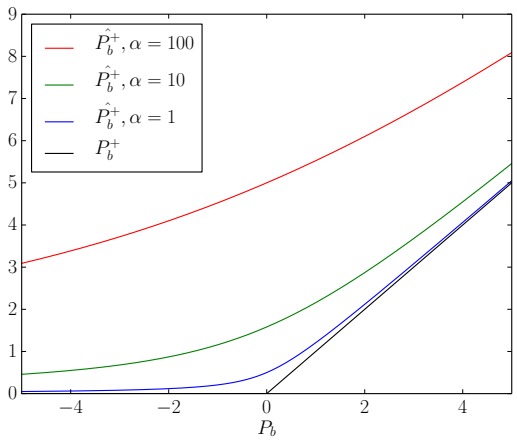

Figure 3: $\hat{P_b^+}$ approaches P_b^+ as α approaches 0.

Unfortunately, the homotopic method is slow, since it requires the computation of a series of optimal trajectories.

Another way to deal with nonsmoothness of the running cost is to reformulate it as a constraint through the addition of variables. This approach is outlined in [29] for dealing with L^1 optimal control problems, where an absolute value function is present in the running cost. For each reaction wheel, a single variable, z_i, is added to the problem formulation. These additional variables have algebraic constraints only, and are therefore treated by the solver the same way as controls. The PRC can then be rewritten using path constraints on z_i as follows:

$$z_i - P_{b,i} \geq 0 \tag{27}$$

$$z_i \geq 0 \tag{28}$$

$$PRC = \sum_{i=1}^{3} z_i \tag{29}$$

In Eq.s 27 and 28, z_i is constrained to be greater than or equal to both $P_{b,i}$ and 0. In Eq. 29, the running cost is defined as the sum of all z_i. In an optimal solution, when $P_{b,i}$ is positive $z_i = P_{b,i}$, since increasing z_i above its minimum allowable value would only increase the cost. When $P_{b,i}$ is negative, $z_i = 0$ for the same reason. Thus, the zeroing of the negative part of the power is reformulated as as a set of constraints on z_i, which solvers are better equipped to deal with. The success of this approach depends on the linear solver used by IPOPT. The best performance is achieved with the HSL MA57 solver [1], and solution time is comparable to that for the TRC (which is relatively independent of linear solver). Use of HSL MA27 [1] and MUMPS [4] linear solvers also yields a solution, but takes several times longer. Use of HSL MA77, HSL MA86, or HSL MA96 [1] does not produce a feasible solution in a reasonable amount of time.

Figure 4 shows solutions obtained using both approaches. There are some slight but noticeable differences between these two trajectories, and the homotopic approach consumes about 2% more energy than the additional variable approach. This is

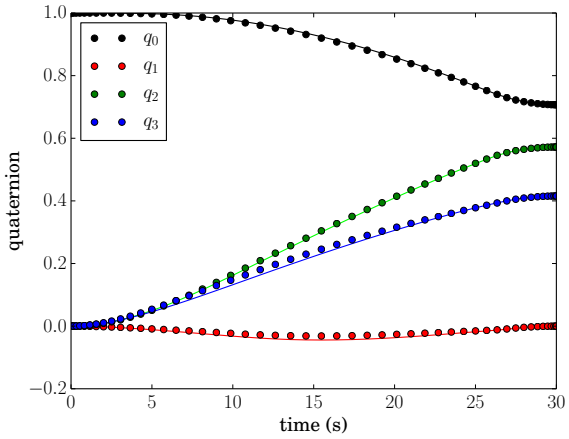

Figure 4: Quaternion trajectories of solutions computed using approximation homotopic approach with $\alpha = 6 \times 10^{-8}$ (solid line) and extra variable approach (dotted line).

due to the fact that the former approximates the PRC, while the latter evaluates it exactly. Due to its superiority in performance and computational efficiency, the extra variable approach is used to generate the rest of the PRC solutions in this document.

2.6.2 Scaling

In his book on numerical optimal control [7], J.T. Betts has the following to say on the subject of scaling: "Scaling affects everything! Poor scaling can a make a good algorithm bad. Scaling changes the convergence rate, termination tests, and numerical conditioning." He then offers some guidelines on how to scale problems, but in general choosing a scaling method is an iterative process. In the simplest terms, scaling is choosing custom units for time, states, controls, and the objective function. Direct optimal control is a numerical method, therefore the performance of algorithms depends on the numerical values of the variables. PSOPT provides automatic scaling routines, outlined in the user manual [5], based on the recommendations in [7], which proved to be sufficient for some, but not all, problems solved in this work. In order to increase reliability, PSOPT's automatic scaling routines were augmented for some of the variables.

The reaction wheel speeds are multiplied by the reaction wheel MOI. Reaction wheels with lower MOI have to go faster to produce the same angular body rate, so trajectories with lower wheel moments have higher values of reaction wheel speed. For the TRC, the objective was scaled by 10^3, since the objective tends to be very small. For the PRC, which produces higher objective values, the objective was scaled by 0.1. In both cases the scaling values were established by trial and error.

When attempting to compute solutions for a broad range of final attitudes, many problems did not converge, and there was no obvious relationship between the final attitude and the occurrence of convergence. It was hypothesized that since the quaternion values range between -1 and 1, they can take on a wide range of orders of magnitude (10^0, 10^{-50}, and $10^{-\infty}$ are all valid quaternion values), which may have caused numerical issues. To combat this, an offset of 10 was introduced, so that the quaternion values would range between 9 and 11. In order to properly determine the quaternion derivative, the offset is removed in the dynamics evaluation function by subtracting 10 from the offset quaternion value before computing $\dot{\boldsymbol{q}}$. Whether this hypothesis is correct or not, this approach did in fact significantly improve the reliability of the solver to over 99.5% when computing the grid of solutions discussed in Chapter 5. Linear interpolation (see section 3.2) was used to produce initial values for the few problems that were not converging, and a 100% solution rate was achieved.

2.6.3 Jitter

The quaternion trajectories returned by PSOPT have a certain amount of jitter (small, random offsets of the values at the collocation points from the true optimum) because the optimization algorithm terminates when it reaches a point that satisfies constraints and optimality conditions within some non-zero tolerance. Tracking a jittery trajectory with a feedback controller (see section 3.1) can produce noticeable increases in energy consumption. To obtain a smooth trajectory, the dynamics can be propagated using a numerical integration method with the computed optimal

control trajectory as input.

3 Optimal Control in Practice

Computation of optimal solutions is not enough: they must be executed by the satellite to be valuable. Since the solutions are based on an imperfect model, using the computed optimal control trajectories to control the satellite directly is likely to yield significant errors. For increased robustness, the optimal solution is tracked using a feedback controller. Additional challenges stem from the fact that optimization is computationally expensive, and generally infeasible to perform aboard the satellite. Solutions can be computed on the ground and radioed up to the satellite, but this is undesireable since it produces communications overhead, and reduces the ability of the satellite to operate independently. Another approach is to precompute a bank of solutions before launch, and use these solutions to reduce computational burden on the satellite hardware.

3.1 Optimal Trajectory Tracking

Perfect modeling of the satellite and controller dynamics is highly improbable, so using the computed motor speeds or torques as input to the controller directly would produce a significant amount of error in the execution, especially in the final attitude. The solution is to use a feedback controller to track the computed attitude trajectory. This is a common approach in practical optimal control [6][18]. Figure 5 presents a block diagram of the tracking controller.

The input to the feedback controller at time t is the value of desired attitude quaternion at that time. $\boldsymbol{q}_e$ is the quaternion error, as defined in Eq. 30, where $\otimes$ is the quaternion multiplication operator, and $*$ is the conjugation operator:

$$\boldsymbol{q}_e = \boldsymbol{q}_1^* \otimes \boldsymbol{q}_2 \tag{30}$$

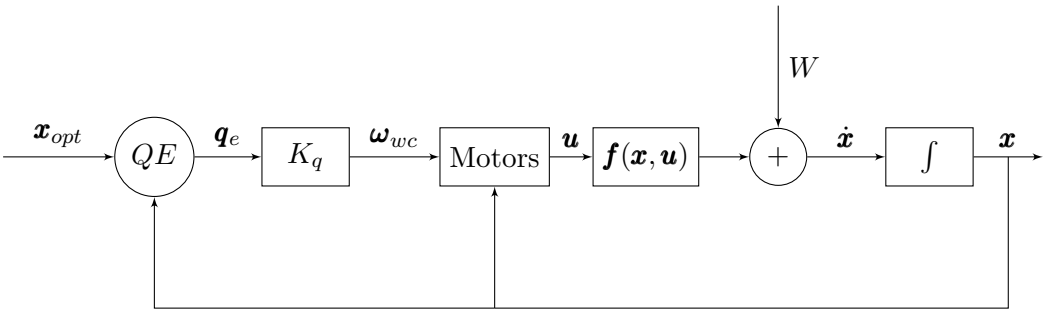

Figure 5: Optimal trajectory tracking feedback configuration

The K_q block is the attitude feedback gain, taking in $\boldsymbol{q}_e$ and generating reaction wheel speed commands, $\boldsymbol{\omega}_{w,c}$. The Motors block models the speed controller and motor dynamics, and its output is the instantaneous torque ($\boldsymbol{u}$). The attitude dynamics are the sum of the modeled dynamics, $\boldsymbol{f}(\boldsymbol{x},\boldsymbol{u})$, and disturbances ($W$), which include external torques, errors in the MOI estimates of the satellite body and reaction wheels, errors in motor parameters, etc. Throughout the majority of this work, the disturbances are assumed to be negligible. The output of the dynamic model, $\dot{\boldsymbol{x}}$, is integrated to produce the current state, $\boldsymbol{x}$, which is fed back to generate quaternion error. The reaction wheel speeds are fed to the feedback speed controller in the Motors block.

The block diagram in Figure 5 assumes perfect knowledge of all states. In reality, these states must be estimated. Attitude and body rate estimation are usually achieved through the fusion of sensor data from an inertial measurement unit (IMU) and an optical attitude sensor, such a sun sensor, earth horizon sensor, or star tracker. Reaction wheel speed measurements are usually implemented using Hall effect sensors or a rotary encoder.

3.2 Autonomous Operation Through Interpolation

The optimal control solver produces an optimal trajectory based on the model specified in the problem definition, at a significant computational cost. The output of a successful optimization routine consists of the optimal values of states and controls at the collocation points, also known as nodes. The compute time for a single solu-

tion depends on the number of nodes. The solutions presented in this work all have 50 nodes, and each takes about a minute to compute on a fifth generation Intel i-7 processor. This level of computational complexity may be beyond the capabilities of a Cubesat's on-board computational hardware. Maneuvers can be computed on the ground and then communicated to the satellite via radio. Both [6] and [18] successfully used this approach. However, it may be desirable for a satellite, especially a Cubesat, to operate semi-autonomously, so as to reduce strain on the communication system and the ground station. Optimal solutions can be precomputed before launch and stored in nonvolatile memory. Because the number of potential maneuvers is infinite, it is impossible to precompute all of them. However, if the entire space of potential maneuvers is sampled with sufficient resolution, it may be possible to compute the solution to an arbitrary problem quickly by interpolating from the nearest neighbors. The feasibility of this approach depends on the nonlinearity of the cost functional and constraints of problem. Fortunately, it is possible to achieve good results using this approach with the system examined in this work. Attitude maneuvers may vary in final attitude (the initial attitude is always defined to be $\boldsymbol{q}(t_0) = [1\ 0\ 0\ 0]^T$), and maneuver time, t_f (t_0 is always defined to be 0).

3.2.1 Final Attitude Interpolation

In chapter 5, a 4851 point grid of solutions is computed, uniformly covering the domain of possible final attitudes. These attitudes are expressed in standard Euler angle form, i.e. $[yaw, pitch, roll]_f$. In order to cover all possible maneuvers, the yaw and roll ranges are $[-\pi, \pi]$, and the pitch range is $[-\pi/2, \pi/2]$. These ranges are covered with a resolution of $\pi/10$, so that there are 21 sample points along the yaw and roll axes, and 11 along the pitch axis. In order to compute a solution to a problem with a new desired final attitude, $[yaw_d, pitch_d, roll_d]_f$, the six nearest neighbors, as measured by euclidean distance between $[yaw, pitch, roll]_f$, are determined. The

quaternion trajectory for the new maneuver is then computed as follows:

$$\boldsymbol{q}_r(t) = \sum_{i=1}^{6} \alpha_i \boldsymbol{q}_i(t) \tag{31}$$

$$\boldsymbol{q}_n(t) = \frac{\boldsymbol{q_r}(t)}{||q_r(t)||} \tag{32}$$

where $\boldsymbol{q}_i$ is optimal trajectory to the final attitude of neighbor i, α_i is the weight $\boldsymbol{q}_i$ receives in the interpolation, and $\boldsymbol{q}_n$ is the interpolated quaternion trajectory. Eq. 32 is a normalization step to ensure that $\boldsymbol{q}_n$ is a valid unit quaternion attitude representation. $\boldsymbol{q}_n$ can then be tracked with the feedback controller.

The interpolation weights are chosen to minimize the error between the desired final attitude and $\boldsymbol{q}_n(t_f)$ by solving the following linear least squares problem:

$$\boldsymbol{\alpha} = \begin{bmatrix} \alpha_0 \\ \vdots \\ \alpha_6 \end{bmatrix} \quad , \quad \boldsymbol{Q} = \begin{bmatrix} \boldsymbol{q}_1(t_f) & \dots & \boldsymbol{q}_6(t_f) \end{bmatrix} \tag{33}$$

$$\boldsymbol{\alpha} = argmin\ [\boldsymbol{Q\alpha} - \boldsymbol{q}_d(t_f)]^T [\boldsymbol{Q\alpha} - \boldsymbol{q}_d(t_f)] \tag{34}$$

Using this method, a quaternion trajectory for an arbitrary final attitude can be computed in a fraction of a second on a simple microcontroller.

To test this approach, one of the grid points is chosen as the target, but that trajectory is not included in the interpolation. Figure 6 plots the PSOPT computed solution for the target point, as well as those of its nearest neighbors to help visualize why the interpolation works. Figure 7 shows the computed solution compared to the interpolated solution. The maximum quaternion error does not exceed 0.004. Note that in Figure 6, the line labeled q_0 is actually $q_0 - 1$, since two identical quaternions will produce a quaternion error of $[1\ 0\ 0\ 0]^T$.

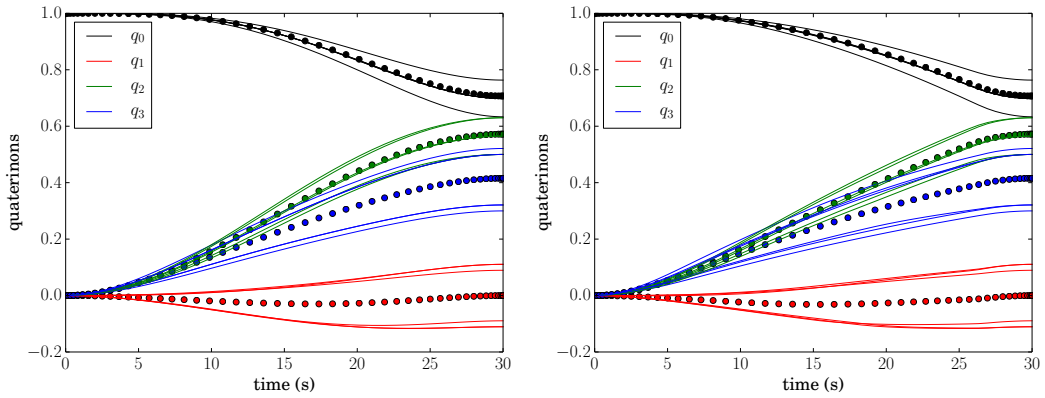

(a) (b)

Figure 6: Optimal quaternion trajectories of target (dotted line) and its six nearest neighbors (solid lines). (a): TRC solutions. (b): PRC solutions.

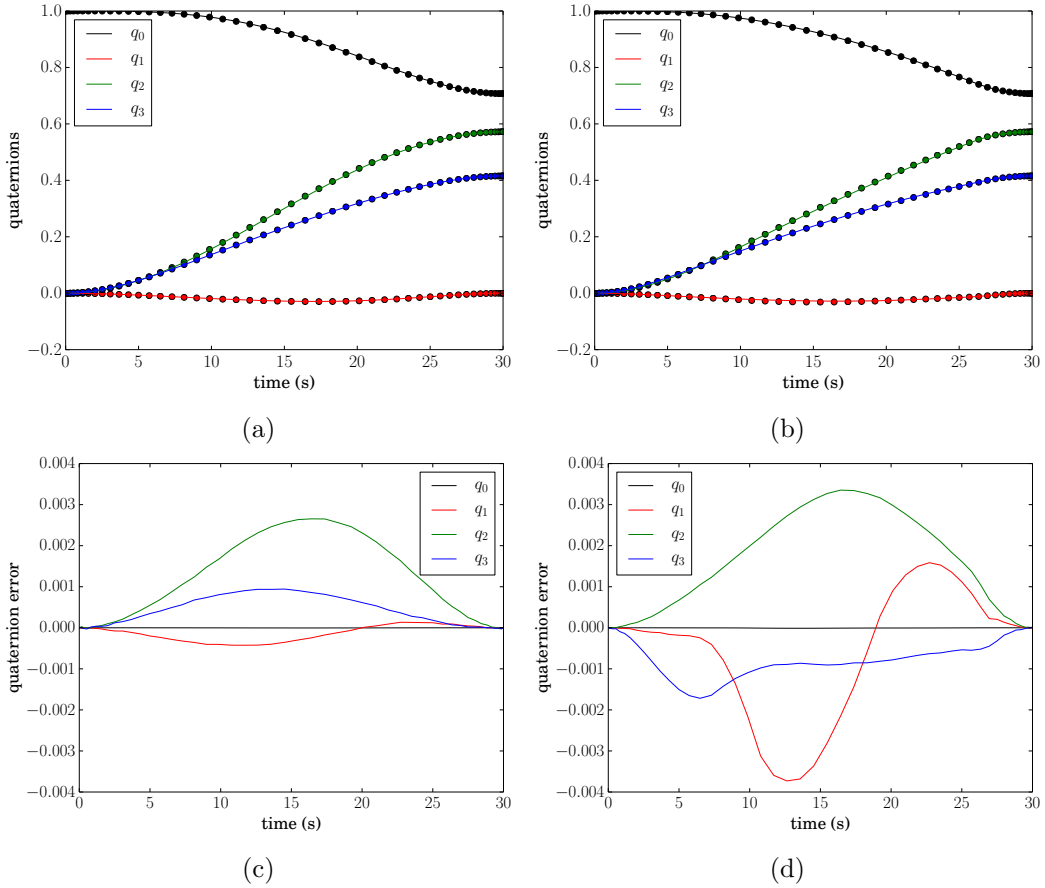

(a) (b)

(c) (d)

Figure 7: (a)(b): Computed (dotted line) and interpolated (solid line) optimal quaternion trajectories. (c)(d): Quaternion error between computed and interpolated trajectories. (a)(c): TRC solutions. (b)(d): PRC solutions.

Once computed, the interpolated trajectory and optimal trajectory are fed into the feedback tracking controller, and the costs (as measured using the nonregenerative braking model in Chapter 2) are summarized in Table 1. The energy values are normalized by that of the PSOPT solution for the TRC. For the PRC, the interpolated solution performs less than 1% worse than the computed solution. In the case of the TRC, the interpolated solution performs slightly better. Because the TRC solution is not optimal with respect the PRC, interpolation errors may produce a solution that has a lower energy consumption. In any case, the interpolation method produces solutions that are very close to those obtained by numerical optimization using PSOPT.

Running Cost	Computed	Interpolated
TRC	1	0.996
PRC	0.807	0.812

Table 1: Summary of normalized energy consumption of computed and interpolated optimal solutions

3.2.2 Time Interpolation

As well as specifying an arbitrary final orientation, users may want to specify an arbitrary maneuver time. To evaluate how maneuvers change as a function of time, a series of 21 optimal maneuvers was computed, with final times ranging between 10s and 100s, distributed evenly on a logarithmic scale. The resultant attitude trajectories are presented in Figure 8, and a benefit of the TRC becomes evident: if the optimal trajectory is computed for a single maneuver time, it can be computed for any other time simply by multiplying the independent variable by the appropriate scaling factor. The PRC solution offers no such convenience; as the final time is varied, the shape of the trajectory changes significantly. Unlike Figure 6, where the neighboring trajectories lie evenly about the target trajectory, the trajectories in Figure 8 cross over each other. Physical interpretations of the results presented in Figure 8 are offered in Chapter 5, where the effects of varying maneuver time are further explored. It appears that time interpolation of the PRC optimal solution

is possible, but may require the computation of a large number of points, which is undesirable because a full attitude grid, as described above, must be computed for each time point. Depending on the application, it may be acceptable to confine the maneuvers to a single time, or a set of several possible times (e.g. a fast time, a medium time, and a slow time). The development of a time interpolation technique for the PRC solutions is left for future research.

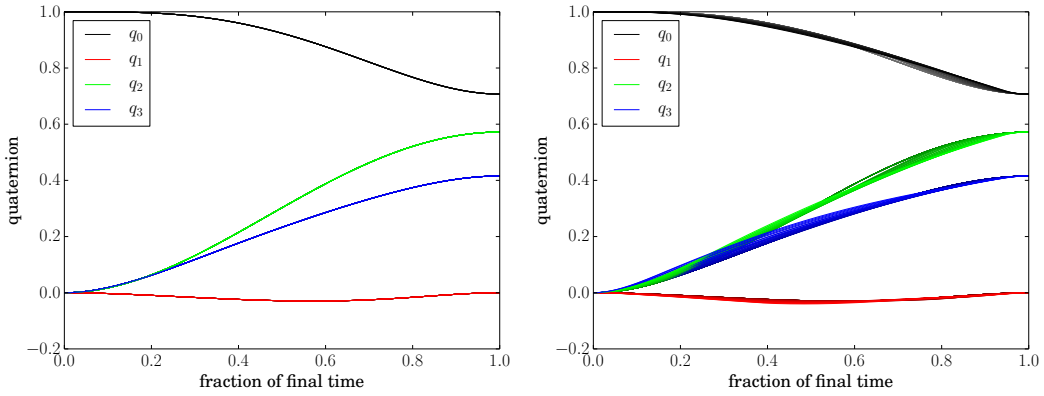

(a) (b)

Figure 8: Optimal quaternion trajectories with different maneuver times plotted on one graph, with fraction of final time on the x axis. Darker lines correspond to longer maneuver times. (a): TRC solutions. (b): PRC solutions.

4 Feedback Tracking Control

Due to disturbances and errors in the estimates of system parameters, driving motors using the optimal control torque trajectories is likely to produce significant errors. Therefore, the execution of optimal maneuvers requires a feedback controller to track the computed trajectories. In this chapter, the effect of varying feedback gains on the energy consumption and tracking accuracy is examined with and without the presence of errors in the body MOI tensor estimate. The feedback controller configuration examined in this section is not unique; other implementations may be better suited to different systems.

4.1 Tracking Controller Configuration

The ability to track a given trajectory requires estimation of the current attitude quaternion and computation of the error. Attitude estimation is beyond the scope of this work, and the availability of a perfect estimate is assumed. Crassidis [11] offers a review of attitude estimation methods. The quaternion error is given by Eq. 35.

$$\boldsymbol{q}_e = \boldsymbol{q}_1^* \otimes \boldsymbol{q}_2 \tag{35}$$

The vector part of the error quaternion ($[q_1\ q_2\ q_3]$) is then multiplied by a constant, k_q, to produce the desired angular momentum vector, expressed in the body frame. A similar approach is used in [18]. Unlike [18], the RWA in this work has three reaction wheels with axes of rotation aligned with the axes of the body frame. Thus, the angular momentum command can be multiplied by another constant, k_h, to produce the reaction wheel speed commands. Because k_q and k_h are both constants they can be combined into a single constant, k_Q.

Speed control of an electric motor is achieved by controlling the duty cycle of the switch mode drive electronics. The duty cycle is usually computed using a PID (Proportional-Integral-Derivative) controller. For the purposes of simulation in this work, the PID controller and motor dynamics are not modeled. Instead, speed control is implemented by multiplying wheel speed error ($\boldsymbol{\omega}_{w,e}$) by a constant, k_ω, and treating the output as the control torque input, $\boldsymbol{u}$, to the dynamic model, $\boldsymbol{f}(\boldsymbol{x}, \boldsymbol{u})$. Figure 9 summarizes the full feedback control system used in the simulation of trajectory tracking.

4.2 Single Axis Linear Model

If rotation is constrained to a single axis parallel to one of the axes of the body frame, then the quaternion error about that axis is $sin(\theta_e)$, where θ_e is the angular distance

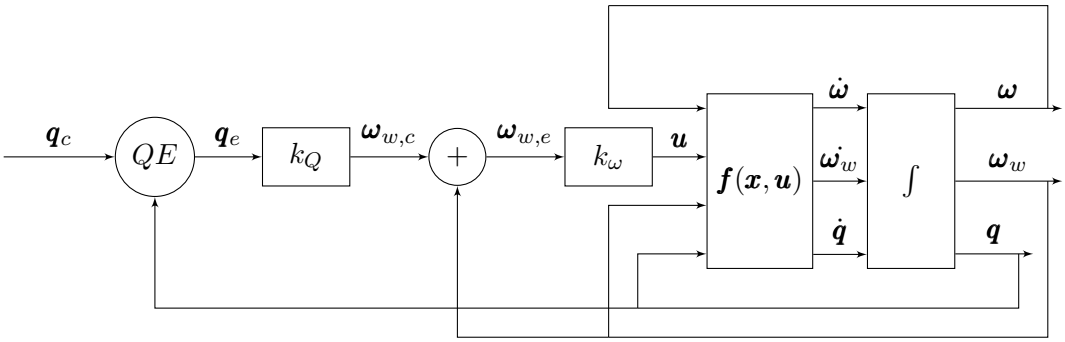

Figure 9: Optimal trajectory tracking feedback configuration.

between the current and desired attitude. Making the small angle approximation $q_e \approx \theta_e$, a simplified one axis linear model of the system in Figure 9 is drawn in Figure 10. Attitude is represented by a single angle, θ. I is the moment of inertia of the satellite body about the axis of rotation. α is the constant relating the angular velocity of the satellite body to that of the reaction wheel, and is given by:

$$\alpha = -(1 + \frac{I}{I_w}) \tag{36}$$

where I_w is the MOI of the reaction wheel about its axis of rotation. α is negative since the reaction wheels rotate opposite the direction of the satellite. k_Q is also negative, for the same reason. u is the torque exerted by the motor on the satellite, not the reaction wheel, so k_w must also be negative.

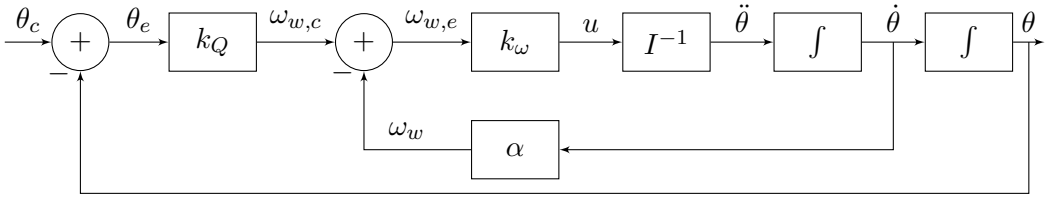

Figure 10: Single axis linear model of Figure 9.

The transfer function of this linear model is:

$$\frac{\theta}{\theta_c} = \frac{\frac{k_Q k_\omega}{s(s+\alpha k_\omega I^{-1})}}{1 + \frac{k_Q k_\omega I^{-1}}{s(s+\alpha k_\omega I^{-1})}} \tag{37}$$

Leaving the transfer function in this form facilitates plotting the 180° root locus as

k_Q varies from 0 to $-\infty$ in Figure 11. Note that since α and k_ω are both negative and I^{-1} is positive, the second pole always lies in the left half plane. Since k_Q is negative, the numerator $k_Q k_\omega I^{-1}$ is always positive, so this is indeed negative feedback, despite the unconventional definition of the feedback gain, k_Q, as negative. It appears that it would be best to choose the highest possible value of k_ω, and choose k_Q as high as it can be without causing oscillation. There are practical limits on the choice of the gains however, including actuator saturation and estimation noise, which can produce highly undesirable behavior if the feedback gains are too high. Furthermore, practical speed controllers are likely to be more sophisticated, and motor dynamics more complex. Still, the linear model provides useful intuition: the quickness of the response of the speed controller has a significant effect on the tracking performance, and choosing k_Q to be too high can cause undesired oscillation.

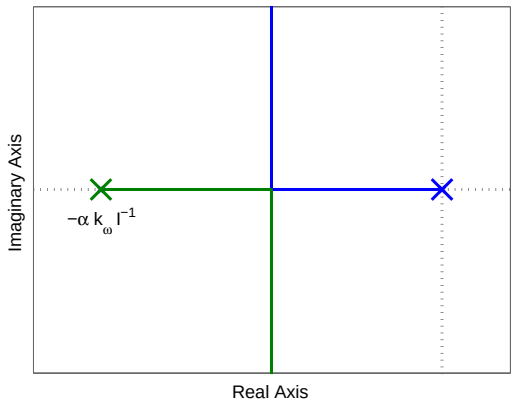

Figure 11: Root locus diagram for single axis linear model.

From Figure 11 it is clear that the system is stable for all negative values of k_Q and k_ω. Increasing the magnitude of k_ω pulls the non-origin pole to the left, allowing for faster settling times. Increasing k_Q is beneficial as it decreases settling time and steady state tracking error. Further increase of k_Q results in departure of the poles from the real axis introducing oscillation in the tracking response.

The other term that affects the location of the nonzero pole is:

$$\alpha I^{-1} = (I^{-1} + I_w^{-1}) \tag{38}$$

Since the MOI of the reaction wheels tends to be much lower than that of the satellite body, I_w^{-1} dominates Eq. 38, indicating that decreasing reaction wheel size improves tracking performance similarly to increasing k_w. Thus, if k_w is limited by estimator noise, decreasing reaction wheel size may improve tracking performance.

4.3 Choosing k_Q

A high value of k_Q produces a controller that more closely tracks the target trajectory and incurs a higher energy cost, as illustrated by Figure 12. As k_Q gets large, the cost converges to the value computed by PSOPT and the error converges to zero, meaning the computed trajectory is being executed perfectly. However, due to estimator noise, it is not advisable to choose a gain that is overly high. An overly high gain may also cause torque saturation in the presence of estimator error and disturbance torques. This effect is not observed in the error free simulation, where the torque exerted by the motors converges to the optimal control torque as k_Q increases. Furthermore, choosing a k_Q that yields a error lower than the accuracy of the estimator is not useful, since a feedback system cannot outperform its measurement capabilities. For the rest of the simulations in this work, we choose $||k_Q|| = 5000$, which produces a final error of less than 0.1 degrees on the evaluated trajectories. This relatively high value is chosen because the main purpose of this work is to evaluate the optimal control approach, so it is desirable that the controller closely tracks the optimal trajectory. On the other hand, it is not so high that it is inconceivable that a real world system could achieve such tracking performance.

4.3.1 A Note About k_ω

$||k_\omega||$ was chosen to be 10^{-4}, and the effects of its variation were not studied extensively, due to the somewhat fictional nature of the simulated motor controller. It was observed that larger values of k_ω produced similar results, while a smaller value (10^{-5}) resulted in significantly decreased tracking performance, as predicted

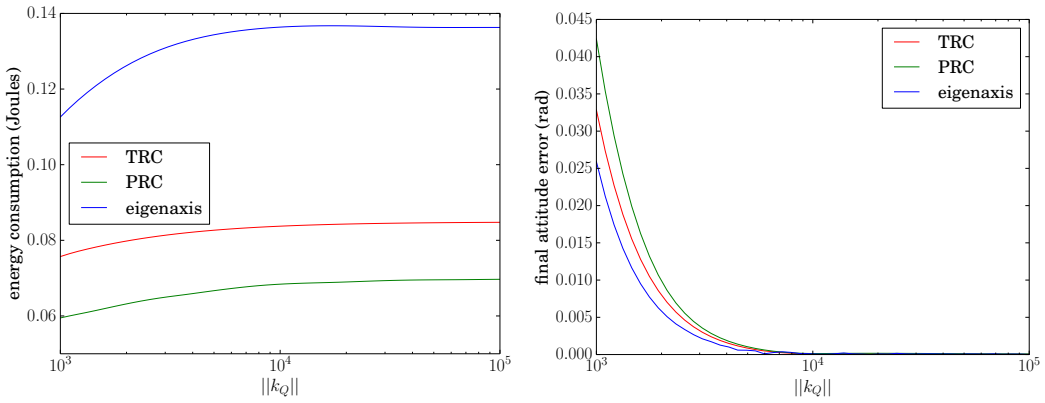

(a) (b)

Figure 12: Effect of varying k_Q on energy consumption (a) and final attitude error (b) for a single maneuver.

by the 1D linear model. Including a better model of the motor dynamics and the speed controller in the optimization and feedback tracking simulation may prove an interesting avenue for future work.

4.4 Effects of Body MOI Estimation Error

Estimation of the satellite body MOI tensor ($\boldsymbol{I}$) is non-trivial. One approach is to model the geometry and mass properties of the satellite using a CAD tool such as SolidWorks, and use numerical methods to estimate the MOI. If the MOI of the reaction wheels is known and their speeds can be measured, then $\boldsymbol{I}$ can be determined experimentally by spinning up the wheels to a known speed and observing the body rate. Use of this approach on the ground is made more difficult by the presence of gravitational torque. $\boldsymbol{I}$ may also be time varying if the satellite has moving parts. In any case, it is inevitable that there will be some error in the estimate of $\boldsymbol{I}$ used in the computation of optimal trajectories, and the purpose of this section is to evaluate the impact of these errors on the performance of the tracked optimal maneuvers.

First, an optimal trajectory was computed using the nominal value of $\boldsymbol{I} = \boldsymbol{I}_{nom}$, as given by Eq. 2, and then the components of $\boldsymbol{I}$ were varied randomly between -10% and 10%, with a uniform distribution and sample size of 100. Simulations of

the tracking of the $\boldsymbol{I}_{nom}$ computed trajectory were performed using the perturbed values of $\boldsymbol{I}$. Then, PSOPT was used to compute the optimal trajectories for the perturbed $\boldsymbol{I}$ matrices. This allowed evaluation of the deterioration of performance of the optimization approach in presence of uncertainty about $\boldsymbol{I}$. In other words, the extent to which an optimal solution obtained using a slightly erroneous $\boldsymbol{I}$ deviated from the true optimal was evaluated by comparing the energy consumption and final attitude error produced by tracking the erroneous maneuver vs the true optimal maneuver. Two metrics are compared in Figure 12, percent increase in energy consumption and increase in final attitude error of using the erroneous trajectory over the optimal trajectory. Examination of Figure 12 reveals that neither performance metric suffers significantly. For the TRC, the increase in energy consumption is often negative since the torque optimal solutions are not optimal with respect to energy consumption. In the case of the PRC, errors in $\boldsymbol{I}$ always produce positive increase in energy consumption, since the PSOPT solutions are energy optimal. The deterioration in final attitude error is small enough to be attributable to integration error, a hypothesis which is supported by the fact that it appears to be normally distributed about 0. In order to visualize the degree of discrepancy in the optimal trajectories in response to small variations in $\boldsymbol{I}$, the 100 optimal solutions for the perturbed $\boldsymbol{I}$ matrices are plotted in Figure 14.

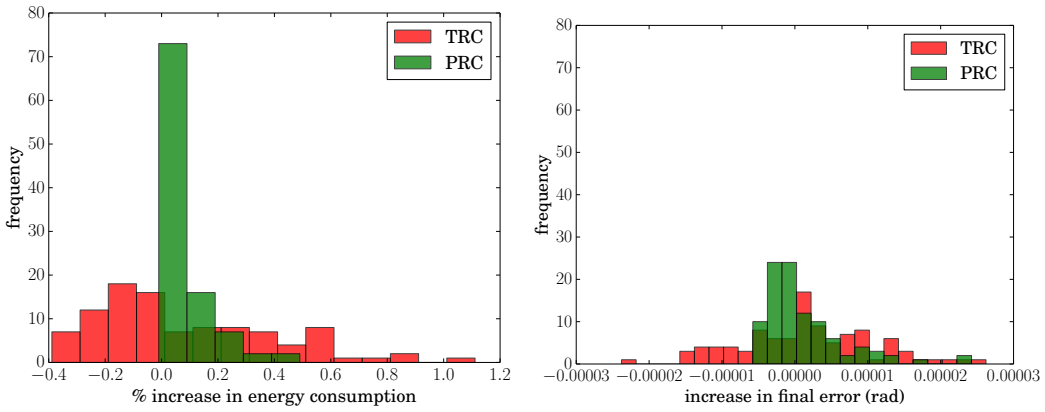

(a) (b)

Figure 13: Deterioration in performance of optimal solution in the presence of errors in the value of I used in optimization. (a): Increase in cost. (b): Increase in final attitude error.

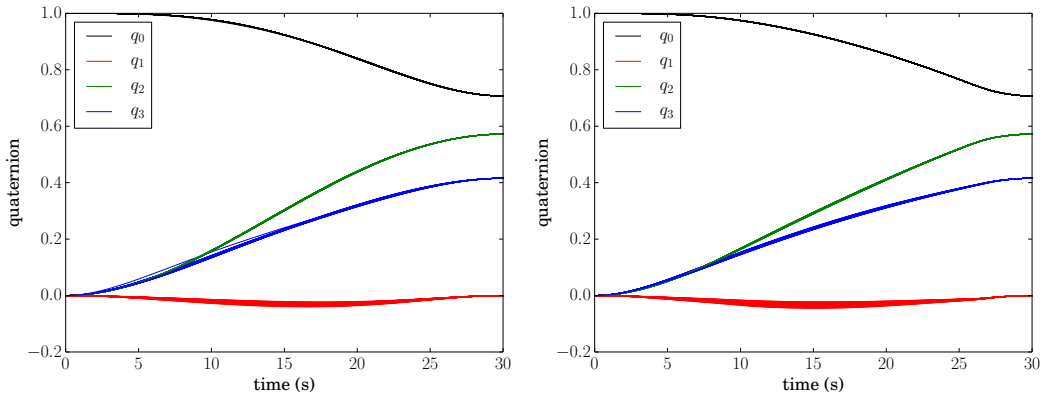

Figure 14: Optimal quaternion trajectories for 100 randomly perturbed I matrices plotted over one another. (a): TRC. (b): PRC.

To ensure that the relationships between $||k_Q||$, energy consumption, and final attitude error found in Figure 12 hold true even with significant errors in the estimate of $\boldsymbol{I}$, the optimal trajectory for the nominal value of $\boldsymbol{I}$ is tracked while the dynamics are propagated using a perturbed value of $\boldsymbol{I}$, $\boldsymbol{I}_p$, as given by Eq. 39 :

$$\boldsymbol{I}_p = \boldsymbol{I} * \begin{bmatrix} 1.1 & 1.04 & 1.3 \\ 1.04 & 1.08 & 1.2 \\ 1.3 & 1.2 & 1.04 \end{bmatrix} \tag{39}$$

where $*$ is the element-wise multiplication operator. Results are presented in Figure 15. It is expected that the relationship between k_Q, energy consumption, and final attitude error will persist as long the computed optimal trajectory remains within the realm of feasible trajectories for the satellite. If the trajectory becomes infeasible, then the energy consumption will climb with k_Q until saturation limits are reached, and the final attitude error will reach a nonzero value. Unless t_f is chosen so that it is close to the minimum possible maneuver time, it is unlikely that the estimate of the body MOI tensor would be so poor as to make the computed trajectory infeasible. Note that simulations presented in all other chapters assume the availability of a perfect estimate of $\boldsymbol{I}$.

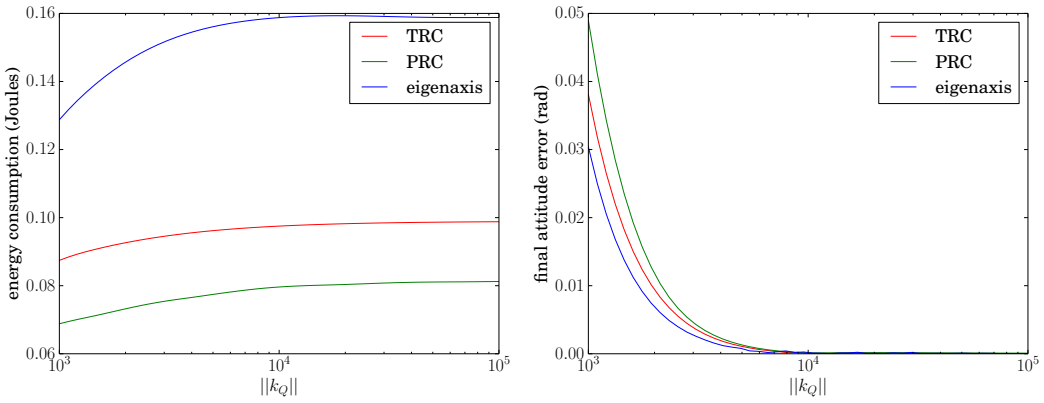

(a) (b)

Figure 15: Effect of varying k_Q on energy consumption (a) and final attitude error (b) for a single maneuver in the presence of significant error in the estimate of $\boldsymbol{I}$.

5 Variation of Parameters

This chapter explores how variation in key parameters (reaction wheel MOI, maneuver time, and maneuver final attitude) affect energy consumption and, more importantly, the relative benefits of the PRC over the TRC, and provides some physical explanations for these relationships. Next, the running costs are compared in a system with differing wheel sizes to demonstrate how the PRC can exploit unusual configurations, expanding the potential of the design. Finally, large grids of solutions with varying final attitudes are computed for several reaction wheel configurations. These grids are necessary for the implementation of the interpolation technique described in Chapter 3. The large grids of optimal maneuvers are compared to eigenaxis maneuvers.

When choosing between the PRC and the TRC, the tradeoff is between efficiency and complexity. Obtaining solutions using the PRC is somewhat more challenging since it requires problem reformulation. It is likely that if additional complexity was added to the problem, such as exclusion zones, the PRC would present even more computational challenges. The solutions produced by the TRC are smooth and it is trivial to extrapolate them to different maneuver times, as was seen in Chapter 3. Furthermore, since the control trajectories of the PRC solution are discontinuous

(see Figure 22), more nodes are required to obtain a solution which is close to the optimum than for the smooth solutions to the TRC. The greater the number of nodes, the greater the computational burden. All solutions presented in this work have 50 nodes, and it is immediately clear upon observation of optimal control trajectories, such as those in Figures 21 and 22, that the TRC optimal solutions are significantly less noisy. In short, TRC optimal solutions are less challenging to obtain and implement. On the other hand, the PRC optimal trajectories always outperform them with respect to the energy metric of Eq. 25, since the PRC yields solutions that are optimal with respect to that metric. The amount of performance improvement obtained using the PRC depends on the attitude control system and the nature of maneuvers it is executing. For example, as will be shown in the next section, if the reaction wheels are large, the PRC does not deliver enough improvement over the TRC to justify the increased complexity of implementation.

5.1 Varying Reaction Wheel MOI

The reaction wheel MOI values were varied between $10^{-6}\ kg \cdot m^2$ and $10^{-4}\ kg \cdot m^2$ at 21 discreet, logarithmically distributed points, with $q_f = [0.71\ 0.00\ 0.57\ 0.42]$ for all runs. The final time was set to $30s$. In order to verify that feasible solutions existed for each value of reaction wheel MOI, time optimal solutions were computed (Figure 16). For the smallest reaction wheel size evaluated, $MOI = 10^{-6}\ kg \cdot m^2$, the minimum maneuver time was about $35s$, so that point was excluded from energy optimization. It is worth noting that $10^{-6}\ kg \cdot m^2$ is approximately the MOI of the motors' rotors without any extra mass attached.

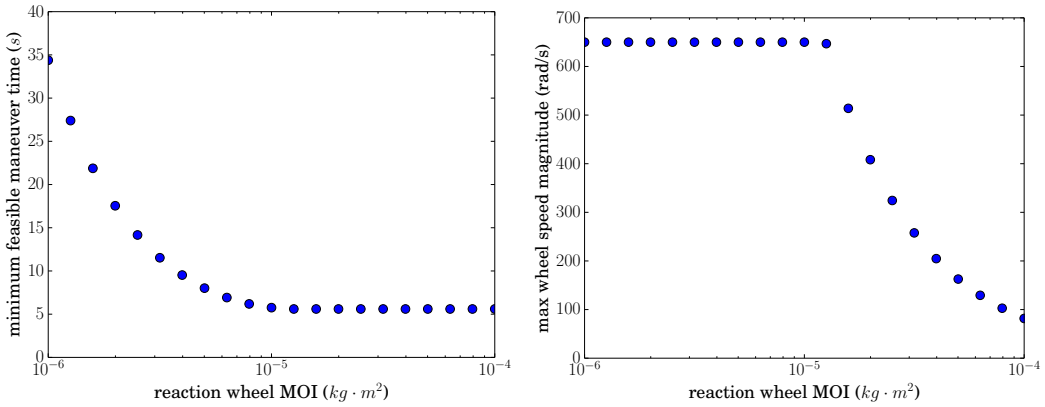

(a) (b)

Figure 16: (a) Minimum maneuver times for varying reaction wheel MOI values. (b) Magnitude of maximum reaction wheel rate attained during maneuver.

Though the focus of this work is energy optimization, Figure 16 offers some interesting insights on the behavior of the time optimal solution as reaction wheel size is varied. For reaction wheel sizes smaller than some threshold, the minimum maneuver time is inversely proportional to the reaction wheel size, while it is constant for reaction wheels larger the threshold. This behavior can be explained by the fact that for smaller reaction wheels, the maneuver time is limited by the maximum wheel speed. With larger reaction wheels, the satellite reaches the final orientation before the wheels can saturate, so the minimum maneuver time is limited by the maximum torque that can be exerted by the motors. The location of this threshold depends on the final attitude; in Figure 16 it lies at approximately $10^{-5}\ kg \cdot m^2$.

Simulation of feedback tracking of optimal solutions allows a more realistic evaluation of their energy consumption and comparison to the eigenaxis maneuver. However, as the reaction wheel size gets small, the tracking error attained by using the feedback configuration in Chapter 4 becomes significant, as illustrated by Figure 18, indicating that higher values of k_Q should be used with smaller wheels. To allow a fair comparison of energy consumption across the full range of reaction wheel sizes considered, the tracking step is excluded here, and energy consumption is evaluated by propagating the computed optimal control trajectory in an open loop fashion. Since the control trajectory is not computed for eigenaxis maneuvers, they are ex-

cluded from this section.

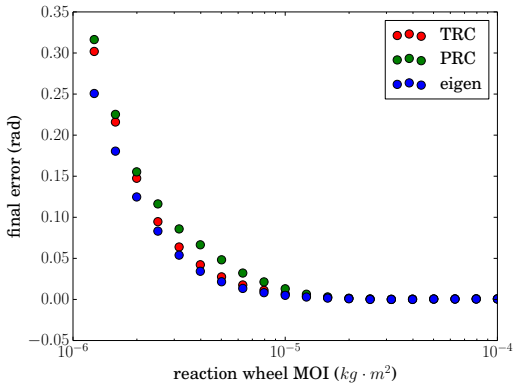

Figure 17: Attitude error at t_f for tracked trajectories.

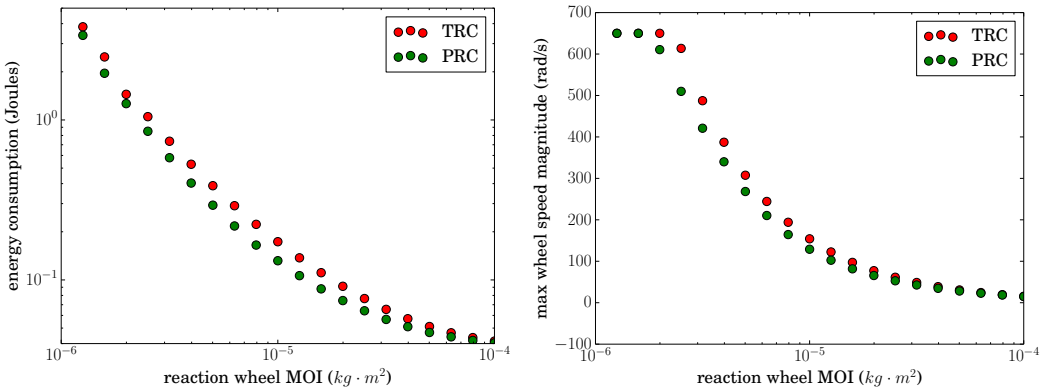

(a) (b)

Figure 18: (a) Energy consumption of optimal maneuvers as wheel MOI varies. (b) Magnitude of maximum reaction wheel rate attained during maneuver.

In Figure 18(a), where the energy consumption of optimal maneuvers is plotted against reaction wheel MOI, it is clear that the smaller the reaction wheel, the greater the energy consumption. This is because smaller wheels must spin faster to produce the same body rate (Figure 18(b)). For example, consider two reaction wheels, one with MOI $= J$ and the other with MOI $= \alpha J$, where $\alpha > 1$. In order to produce the same body rate, they must produce the same angular momentum, H, and the kinetic energy stored in the smaller wheel must be α times greater, as shown by Eq.s 40 through 46. Since this kinetic energy is unrecoverable in the absence of regenerative braking, maneuvering with smaller wheels is more expensive. The effects of dynamic friction also contribute to this trend, as reaction wheels which

spend more time spinning quickly will experience greater frictional losses.

$$H_1 = J\omega_1 \ , \quad E_1 = \frac{1}{2}J\omega_1^2 \tag{40}$$

$$H_2 = \alpha J\omega_2 \ , \quad E_2 = \frac{1}{2}\alpha J\omega_2^2 \tag{41}$$

$$J\omega_1 = \alpha J\omega_2 \tag{42}$$

$$\omega_1 = \alpha\omega_2 \tag{43}$$

$$E_2 = \frac{1}{2}\alpha J(\frac{\omega_1}{\alpha})^2 \tag{44}$$

$$E_2 = \frac{1}{2\alpha}J\omega_1^2 \tag{45}$$

$$E_1 = \alpha E_2 \tag{46}$$

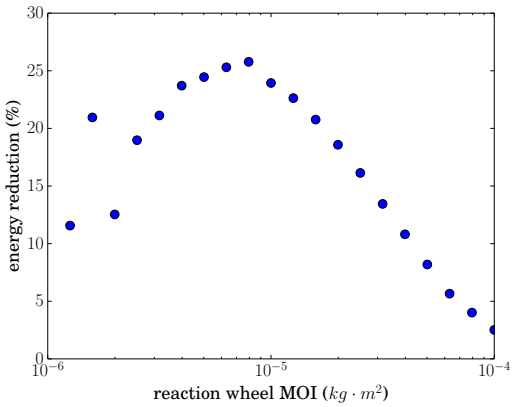

Figure 19: Reduction in energy consumption of PRC over TRC.

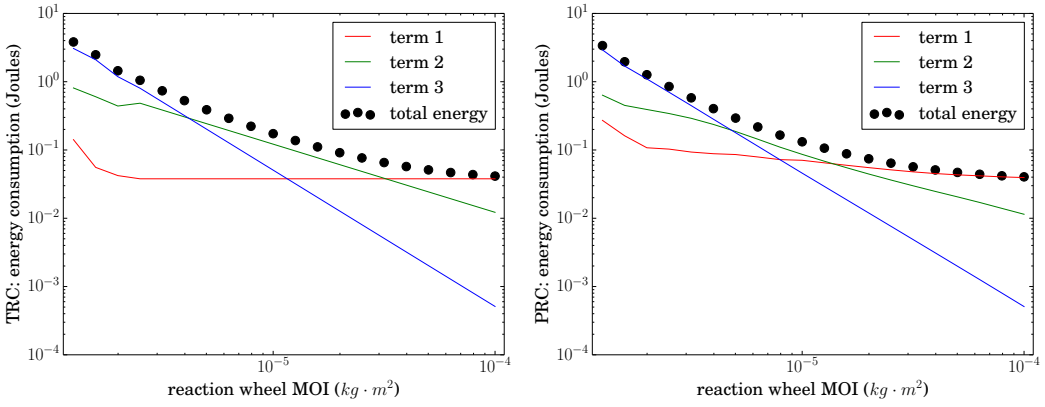

(a) (b)

Figure 20: Energy consumption broken down by the three terms of Eq. 23 for PRC and TRC optimal solutions as reaction wheel MOI is varied.

Figure 19 plots the percent reduction in energy consumption of PRC solutions over TRC solutions. To help explain the shape of this curve, the contribution of the three terms of Eq. 23 are plotted separately in Figure 20. If the second term was propagated unmodified, it would integrate to 0, since the initial and final kinetic energies are both 0. Thus, to account for the amount of unrecoverable mechanical energy injected into the reaction wheel, $0.5 \times ||term2||$ was propagated to generate the line labeled term 2 in the figure. Propagating each term independently and summing does not produce the real energy consumption, since the real power is computed by summing the three components and then setting the sum to zero if it is negative. Physically, this is because the stored kinetic energy can be used to decelerate the wheel without injecting extra current. The purpose of Figure 20 is to give a sense of the magnitudes the three terms, and approximately how much they contribute to energy consumption. It is observed that the improvement becomes small as the reaction wheel size gets large. This is due to the fact that the second and third terms of Eq. 23 depend on the reaction wheel velocity. For maneuvers with large wheels, the wheel velocities are small, so the second and third terms become negligible, the first term dominates, and the TRC and PRC become equivalent. The improvement in Figure 19 also gets smaller as the reaction wheels become very small because both solutions begin to approach the time optimal solution, i.e. as the reaction wheel size approaches the threshold for feasibility for the given maneuver time, just satisfying the constraints requires so much actuation effort that there is little opportunity left for optimization. The third, and perhaps most salient, feature of Figure19 is that the second and third points from the left seem to deviate from what is otherwise a fairly smooth curve. This can be explained through examination of Figures 21 and 22, which plot the computed optimal control trajectories for the TRC and PRC, respectively.

The plots in Figure 22 show the PRC optimal control trajectories for four different values of reaction wheel MOI that span across the entire range under consideration, and they all have similar shapes. Initially, there is an acceleration phase, then a "coast" phase, where the applied torque is small, and finally a sharp deceleration

phase. As the reaction wheel size gets smaller, the acceleration and deceleration phases get shorter and more aggressive, and the coast phase becomes longer. Understanding why the PRC optimal trajectory has this form is facilitated by considering a one dimensional system. In order to get from the initial to final angle in the given amount of time, the system must achieve a fixed average velocity. To minimize unrecoverable mechanical energy while meeting this constraint, the PRC optimal solution needs to minimize the maximum speed attained by the reaction wheels, which it achieves by quickly accelerating and then coasting. This also serves to minimize frictional losses, which grow quadratically with reaction wheel speed. However, the first term in Eq. 23 penalizes the exertion of control torque, effectively limiting the magnitude of the acceleration and deceleration torque spikes. As the reaction wheels get smaller, the second and third terms dominate, and the torque spikes get larger. When the reaction wheels are large and the first term dominates, the PRC and TRC optimal solutions look similar (compare Figure 22(d) and 21(d)). The deceleration is always more aggressive than the acceleration because deceleration does not consume energy as long as Eq. 23 remains negative, which is why the optimal solution limits the magnitude of the deceleration spike. Even as the reaction wheels begin to saturate, the nature of the PRC optimal solutions doesn't change significantly. The acceleration and deceleration spikes just get higher and narrower, since the reaction wheels need to maintain their maximum velocity longer as they get smaller in order to satisfy the requirement on average body rate.

The TRC optimal solutions, on the other hand, remain exactly the same as long as the reaction wheels don't saturate (Figure 21(d)), since the TRC does not include any terms that penalize the reaction wheel speeds. However, once the reaction wheels do get small enough to saturate, the shape of the TRC optimal solution has to change radically (Figure 21 (a)-(c)) in order to satisfy the requirement on average body rate, and begins to look more like the PRC optimal solution, with sharper acceleration and deceleration spikes and a coast phase. As the reaction wheel MOI reaches the limit of feasibility for the given time, both TRC and PRC solutions will look the same as the time optimal solution. The transition phase of the TRC causes

the spike in Figure 19.

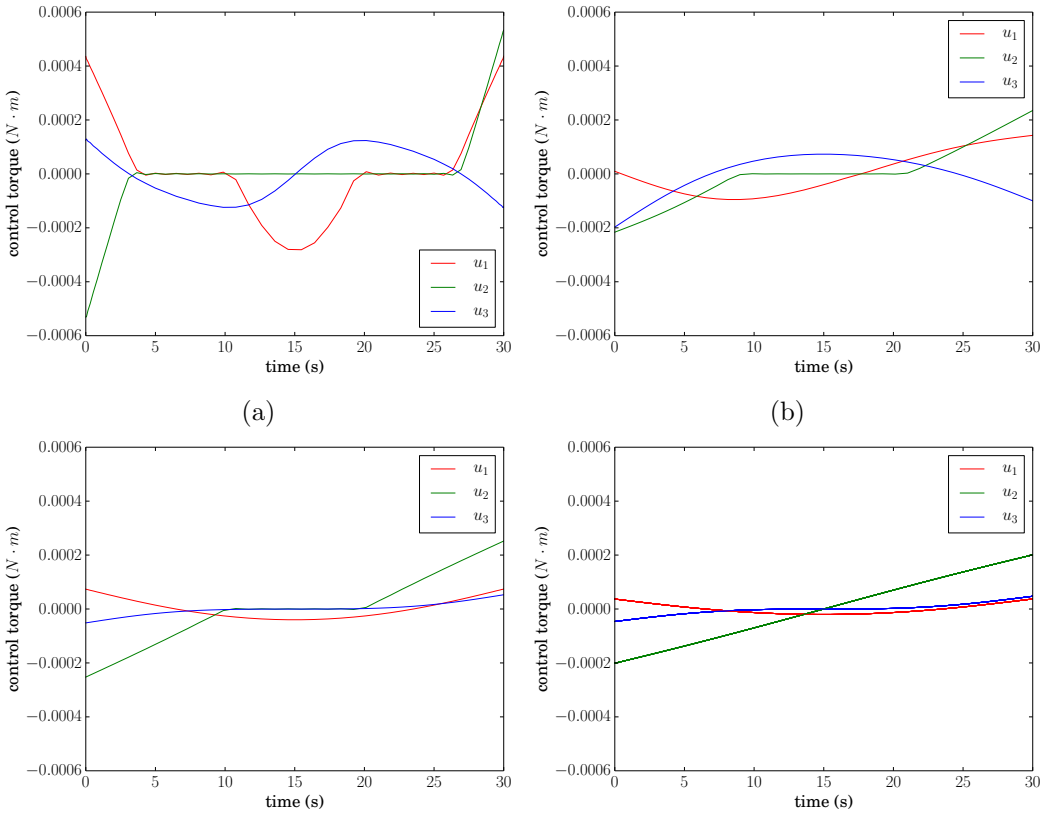

Figure 21: TRC optimal control trajectories for all points in Figure 19. (a) First point from the left. (b) Second point from the left. (c) Third point from the left. (d) All other points plotted on top of each other.

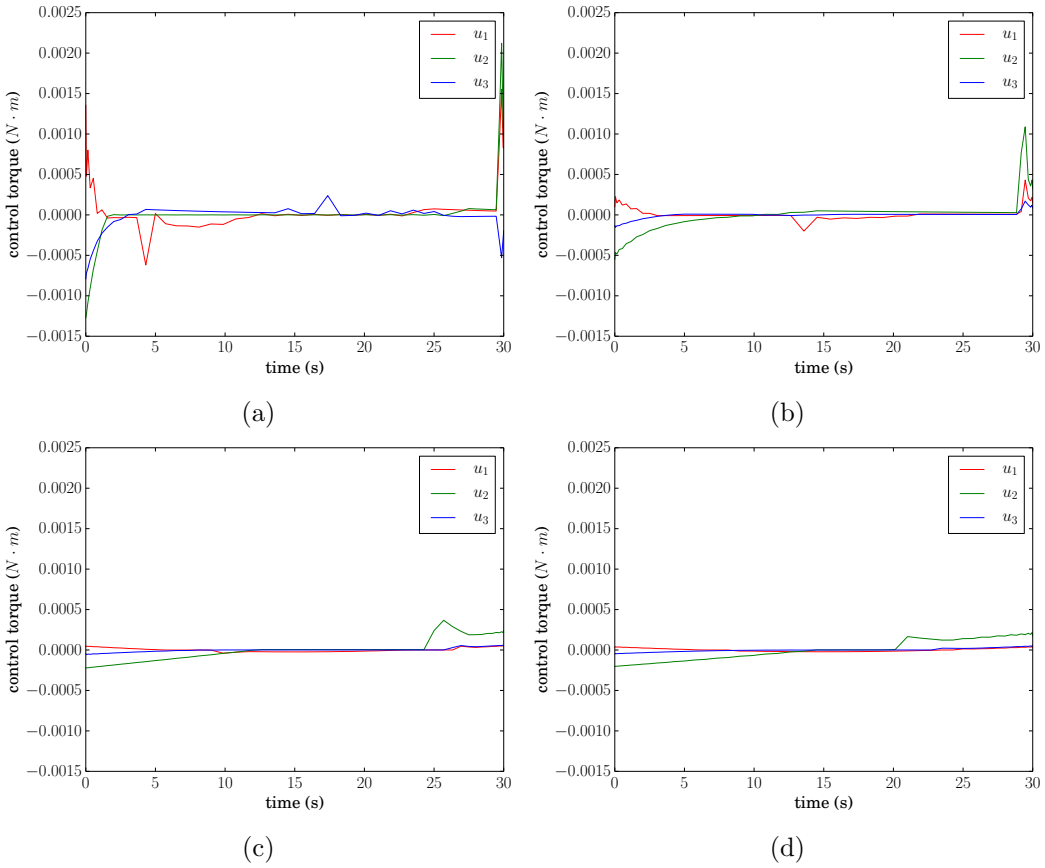

Figure 22: PRC optimal control trajectories for four points in Figure 19. (a) First point from the left. (b) Sixth point from the left. (c) Sixteenth point from the left. (d) Twentieth point from the left.

5.2 Varying Maneuver Time

In this section, the reaction wheel MOI is held fixed at $2.2 \times 10^{-5} kg \cdot m^2$, which is the MOI of a commercially available Cubesat reaction wheel [2]. The final attitude of the maneuver is the same as that in used in the previous section. From Figure 16, it is known that the minimum time for this maneuver is approximately 5.5 s. Therefore, the shortest maneuver time examined is 6s, and the longest is 600s. Energy consumption for 21 values of t_f, distributed logarithmically between the two extremes, is plotted in Figure 23(a). As in the previous section, the feedback tracking is not simulated, and the eigenaxis trajectory is not included for comparison. The reaction wheel speeds do not saturate during any of the maneuvers (Figure 23(b)), which is unsurprising since the reaction wheel MOI is large enough that even the

time optimal maneuver doesn't saturate the reaction wheel speeds (refer to Figure 16(b)). The energy reduction achieved by using the PRC over the TRC is plotted in Figure 24. Figure 25 presents the cost breakdown, similar to Figure 20. For short maneuver times, the energy reduction of the PRC over the TRC is very small, tending towards zero as both solutions converge on the minimum time solution. Since the factor limiting the minimum maneuver time is torque, solutions to both cost functionals must produce very high torques, and the first term, proportional to the square of torque, dominates. For medium length maneuver times, the second term, unrecoverable mechanical energy, is significant for both solutions, but smaller for the PRC since the PRC attempts to minimize it. In this range, energy reduction is at its maximum. For long maneuver times, the torques exerted and maximum wheel speeds are low, so the third term, friction, dominates, and the PRC starts to lose some of its edge, since the unrecoverable mechanical energy becomes relatively insignificant. Since the PRC accounts for frictional losses as well, the improvement curve begins to flatten out at very long maneuver times. At this point, the energy consumed by both maneuvers is very low.

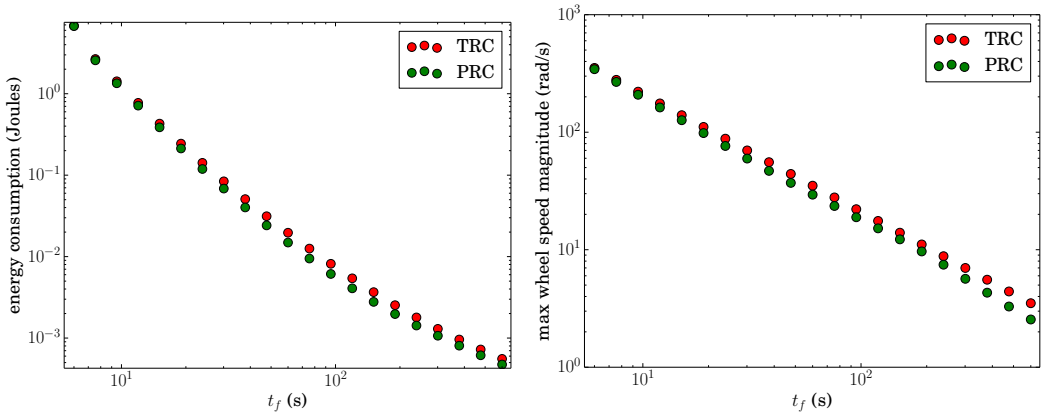

(a) (b)

Figure 23: (a)Energy consumption of maneuvers for varying values of t_f. (b) Magnitude of maximum reaction wheel velocity attained during maneuver.

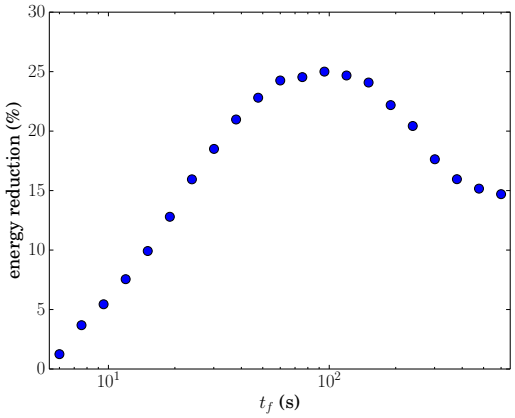

Figure 24: Reduction in energy consumption of PRC solution compared to TRC solution

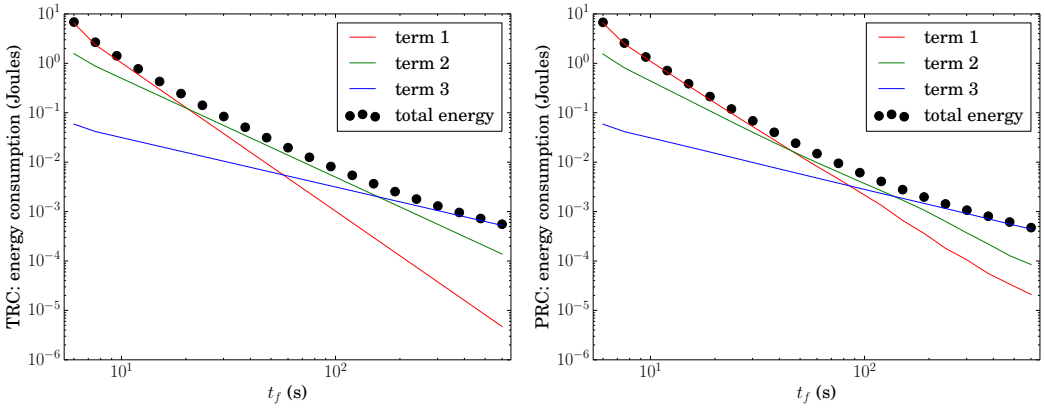

(a) (b)

Figure 25: Energy consumption broken down by the three terms of Eq. 23 for TRC and PRC optimal solutions as t_f is varied.

The improvement curve for the time varying case did not have a spike like the one in Figure 19, because the reaction wheel value is large enough that reaction wheel speed saturation never occurs. Torque saturation does occur for short maneuver times (Figure 26 (a) and (b)), but does not cause radical changes in the optimal control because the TRC always attempts to minimize torque, with or without saturation. On the other hand, when reaction wheel speed saturation occurs, the TRC optimal maneuver has to change significantly, since it now has to account for a new variable.

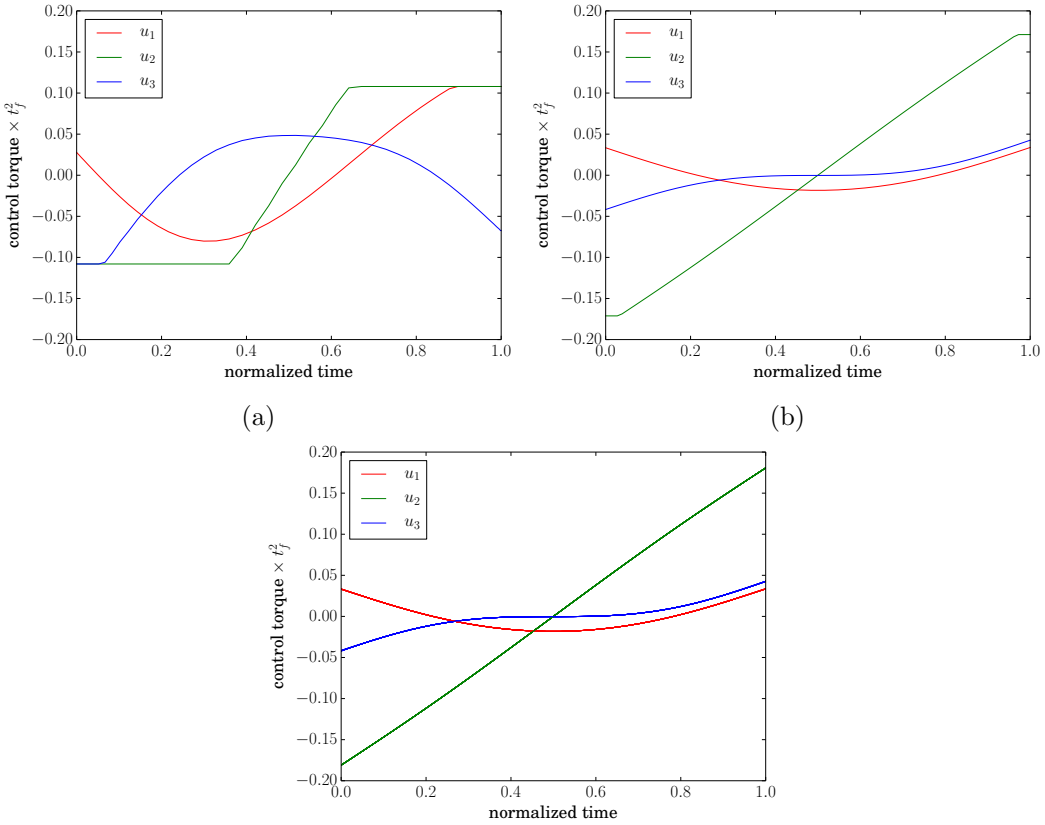

Figure 26: TRC optimal control trajectories with torques multiplied by t_f^2 and normalized independent variable, for all points in Figure 24. (a) First point from the left (saturation). (b) Second point from the left (saturation). (c) All other points (no saturation).

In Figure 8, it was observed that if the independent variable was normalized the quaternion trajectories of the TRC optimal solutions for varying maneuver times looked identical (as long as saturation was avoided). In order to make the optimal control trajectories look identical, it was found that the control torques needed to be multiplied by t_f^2, in addition to normalization of the independent variable (Figure 26(c)). As an explanation of this inverse linear dependence of the optimal control torque on t_f^2, the analytical solution to the 1 dimensional TRC problem is derived in Appendix A and given by Eq. 47:

$$u = -12\frac{\theta_f}{t_f^2}\left(\frac{t}{t_f} - \frac{1}{2}\right) \tag{47}$$

The t/t_f term in Eq. 47 is the normalized independent variable in Figure 26. It is apparent that for a given final orientation, the optimal control scales linearly with the inverse of square of t_f. Figure 26(c) confirms that this relationship holds in the three axis case.

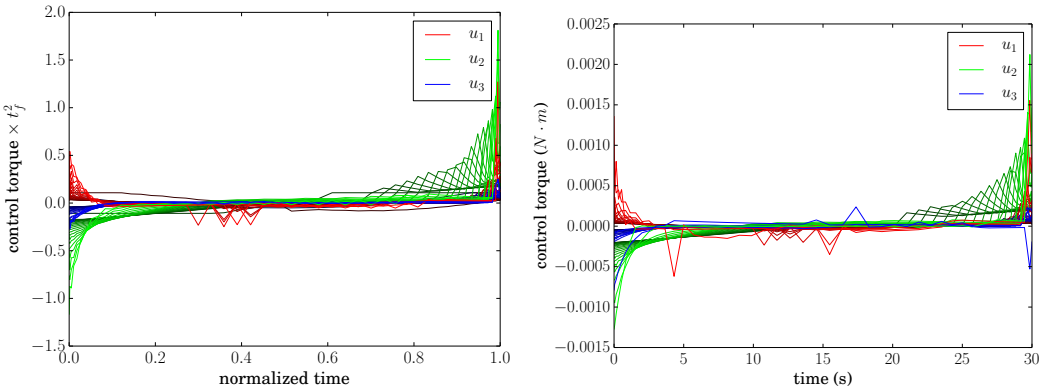

(a) (b)

Figure 27: Many PRC optimal control trajectories plotted together. (a) t_f varied, brighter line corresponds to longer maneuver time. (b) Reaction wheel MOI varied, brighter line corresponds to smaller reaction wheel.

Applying the same transformation to the PRC optimal solutions for varying t_f and superimposing on one plot yields Figure 27(a). Figure 27(b) superimposes all optimal control trajectories obtained by varying wheel size, and the two plots look nearly identical. It appears that the shape of the PRC optimal control trajectory changes similarly for decreasing wheel size as it does for increasing maneuver time. This may be somewhat surprising, but it must be remembered that the magnitude of the controls in Figure 27(a) are multiplied by t_f^2. In fact the trajectories with the smallest magnitudes in Figure 27(a) are actually the greatest control torques. The reason for this trend is that when the maneuver time is long, terms 2 and 3 dominate, so it makes sense to accelerate the wheels relatively quickly so as to minimize the maximum speed that has to be achieved. For varying reaction wheel size, terms 2 and 3 dominate when the reaction wheel size is small, producing the same behavior.

5.3 Varying Final Attitude

In this section, the maneuver time is held constant at $30s$ (unless otherwise specified) and the reaction wheel MOI is set to $2.2 \times 10^{-5}\ kg \cdot m^2$. The final attitude is varied in two ways: first the axis of rotation is held constant while the magnitude is varied, and then the axis is varied as the magnitude is held constant.

To generate Figure 28, the axis of rotation is set to $\boldsymbol{e} = [0.00\ 0.81\ 0.59]$ and the maneuver angle (θ) is varied between $\frac{\pi}{10}$ and π. The cost breakdown is computed in the same manner as for Figure 20. As expected, the energy consumption of the maneuver increases with increasing θ. The first two terms of Eq. 23 dominate, as the reaction wheel speeds are not high enough to create significant frictional losses. The percent energy reduction achieved using the PRC over the TRC is plotted in Figure 29, for three values of t_f. The variation in improvement is slight for all t_f. In Figure 25, the dominating term changed as t_f was varied, leading to significant variation in energy reduction. In contrast, as θ is varied, the relative importance of the terms remains approximately constant, resulting in small variation.

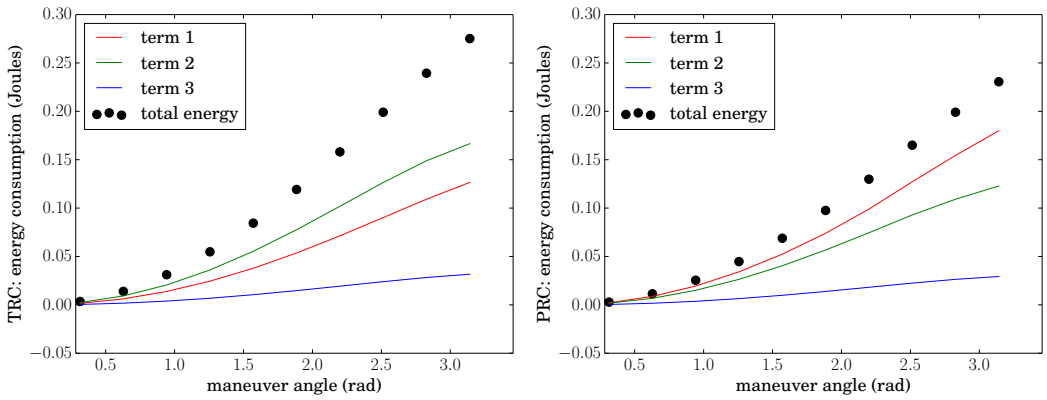

(a) (b)

Figure 28: Energy consumption broken down by the three terms of Eq. 23 for TRC and PRC optimal solutions as maneuver angle is varied.

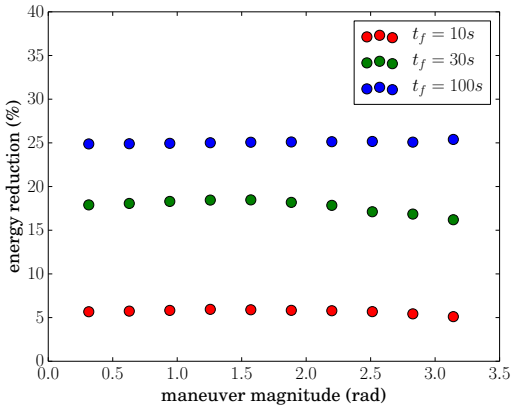

Figure 29: Percent energy reduction of PRC over TRC as the maneuver angle varies for three values of t_f.

In Figure 30, maneuver angle is held fixed at $\theta = \frac{\pi}{2}$. The x component of the rotation axis is set to 0. The z component of the rotation axis is varied between 0 and 1, and the y component is set so that the magnitude of the rotation axis vector is 1. Since the MOI of the spacecraft about the z axis is several times smaller than those about the x and y axes, it is expected that the maneuver costs will decrease with increasing z axis component. The results in Figure 30 confirm this expectation. The extent of energy reduction with increasing z axis component is significant: the rotation about the y axis consumes over 20 times more energy than that about the z for both TRC and PRC, though the MOI about the y axis is only 5 times greater than that about the z axis. The percent energy reduction using the PRC over the TRC is plotted in Figure 31, and the variation is not large. Since the variation in energy reduction is small as both the rotation angle and axis of rotation vary, it is reasonable to expect the results from the previous two sections to remain applicable across the full range of final attitudes.

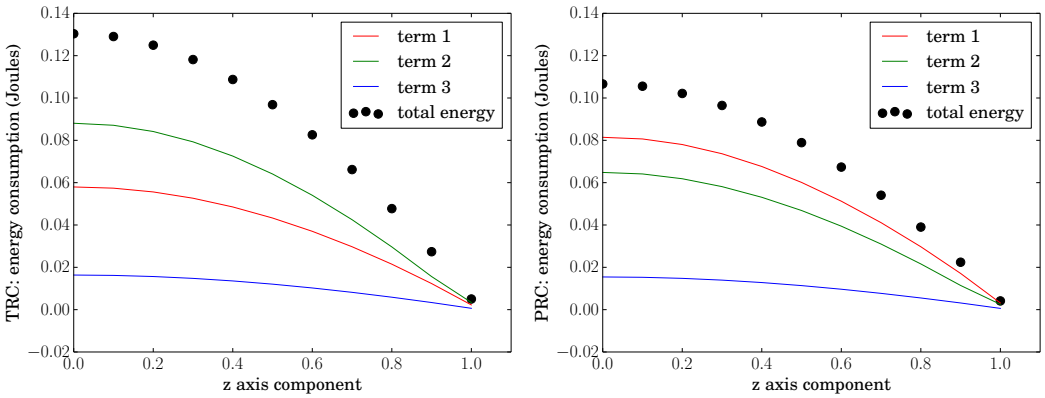

(a) (b)

Figure 30: Energy consumption broken down by the three terms of Eq. 23 for TRC and PRC optimal solutions as the z component of the rotation axis is varied.

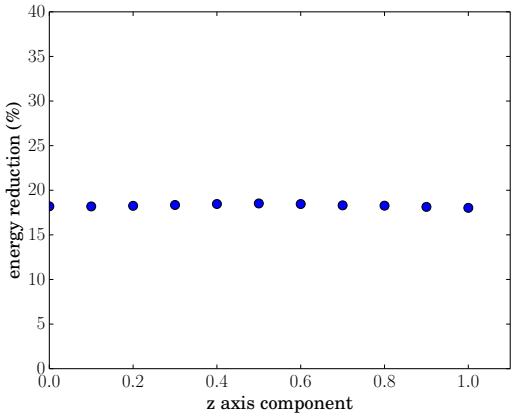

Figure 31: Percent energy reduction of PRC over TRC as the z component of the rotation vector varies.

5.4 Differently Sized Wheels

In some cases, it may be advantageous to have reaction wheels with different MOI. For example, if the majority of a satellite's maneuvers are about a certain axis, placing a large reaction wheel on that axis could significantly reduce energy consumption, while large reaction wheels on the other axes may be unnecessary. It may also be that the geometry of the spacecraft and its subsystems allows for one wheel to have a large radius without increasing the bulk of the attitude control system. Since the TRC does not account for wheel speed unless saturation occurs, the potential for

improvement by using the PRC is significant. The reaction wheel MOI is set to 1×10^{-4}, 1×10^{-5}, and 1×10^{-5} $kg \cdot m^2$ for the x, y, and z wheels respectively. The maneuver axis and angle are varied in the same fashion as in the previous section, because it is expected that the energy reduction will have a strong dependence on the final attitude.

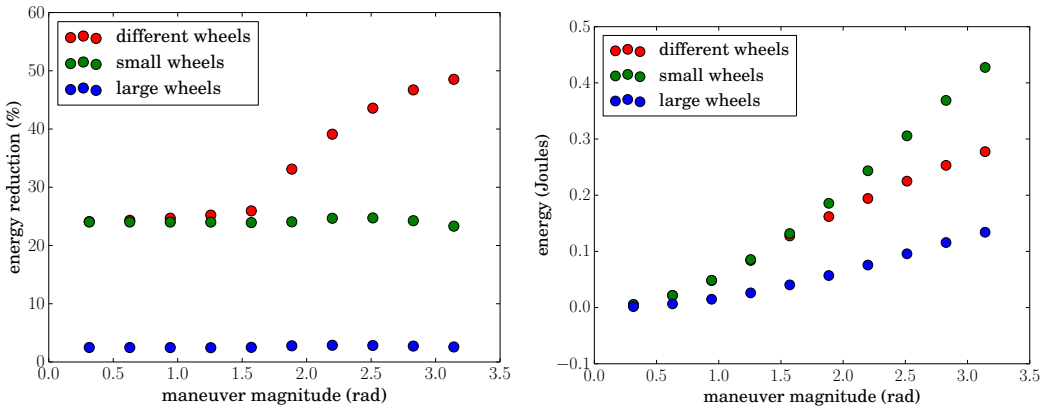

(a) (b)

Figure 32: Variation of maneuver angle for three reaction wheel configurations. Wheel MOI are (in $kg \cdot m^2 \times 10^{-5}$): different wheels = [10 1 1], small wheels = [1 1 1], large wheels = [10 10 10]. (a) Percent energy reduction using PRC over TRC. (b) Energy consumption of PRC optimal solutions.

In Figure 32(a) energy reduction of PRC over TRC solutions is plotted for three reaction wheel configurations as θ is varied and the rotation axis is kept constant at $\boldsymbol{e}$ = [0.00 0.81 0.59]. The first is the configuration with differing wheel sizes as described above. The next one is a configuration where all wheels are the same size, with MOI equal to that of the small wheels in the differing wheel size configuration. The last one has three uniform wheels with MOI equal to that of the large wheel of the different wheel size configuration. Notice that the x component of the rotation axis, which is the axis with the big wheel, is zero. It is observed that for maneuver angles smaller than $\frac{\pi}{2}$ rad, the improvement for different wheels is nearly identical to that of the uniform small wheels, but above $\frac{\pi}{2}$ rad the improvement rises rapidly and ultimately reaches 50% at $\theta = \pi$ rad. The reason for this radical shift is best explained by examining the body rate trajectories in Figure 33. In (a) and (b), where $\theta = \frac{\pi}{2}$, the majority of the angular rate is allocated to the y and z axes and

therefore the y and z wheels. This results in a maneuver that is somewhat similar to the eigenaxis maneuver; the larger a component of the rotation axis, the larger that component of the angular velocity. In (c), which is the TRC solution with $\theta = \pi$, more or less the same pattern is observed: the y and z wheels spin quickly and the x wheel spins slowly. On the other hand, the maneuver in (d) is very different. Notice that the y axis component of body rate is very small. Instead of rotating about the y axis, the satellite first rotates about the z axis (which is relatively inexpensive since the MOI about the z axis is low) so that the body x axis becomes aligned with the inertial y axis. Next, the satellite rotates about its x axis, incurring low penalties since the x reaction wheel is large, and then back around its z axis to put all the body axes in the correct orientation. Of course, in reality this is not executed in stages, but as a single, smooth maneuver. This exploitation of the non-uniformity of the reaction wheels allows for a 50% energy reduction over the TRC, which does not account for reaction wheel speeds. For maneuvers with $\theta \leq \frac{\pi}{2}$, the growth rate of the PRC cost with θ is the same for the different wheels as it is for the small wheels, but for θ greater than this threshold the growth rate is close to that of the large reaction wheels (Figure 32 (b)).

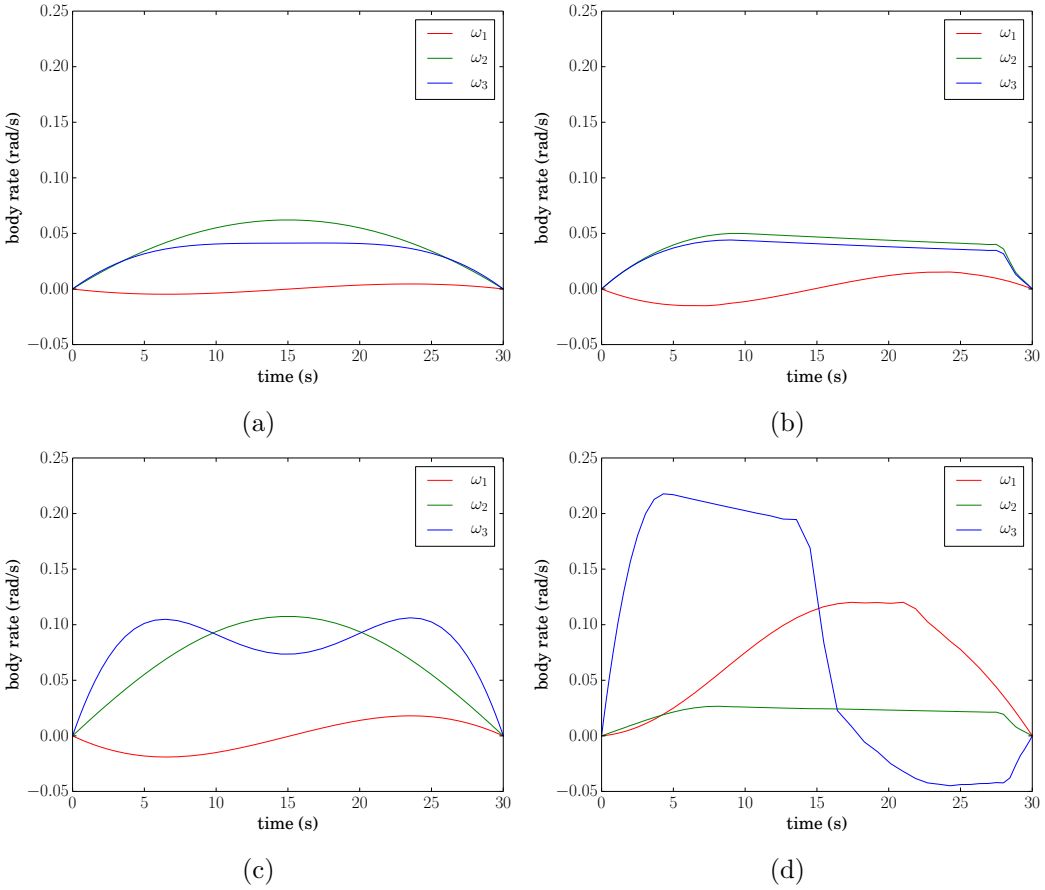

Figure 33: Optimal body rate trajectories for control system with differently sized reaction wheels. (a) TRC optimal $\theta = \frac{\pi}{2}$. (b) PRC optimal $\theta = \frac{\pi}{2}$. (c) TRC optimal $\theta = \pi$. (d) PRC optimal $\theta = \pi$.

Similar to the previous section, the magnitude of the z component of the rotation axis is varied while θ is maintained constant. Since the previous analysis showed that the PRC behaves differently when $\theta > \frac{\pi}{2}$, this process is performed for two values of θ: $\frac{\pi}{2}$ and π. The results, which are computed for the three reaction wheel configurations from the previous analysis, are presented in Figure 34. As in the uniform wheel size case, the energy consumption of the maneuver decreases with increasing z-axis component. For the two uniform wheel size configurations, the energy reduction is nearly independent of the z component for both θ values. When $z = 1$, the energy reduction is the same for the different wheels and the small wheels, since the x axis wheel is unused in both cases. In (c), there is a noticeable jump between $z = 0.6$ and $z = 0.7$, which is attributed to a change in maneuver modalities; the same as the one

that occurred when the maneuver angle passed $\frac{\pi}{2}$ in Figure 32. This is confirmed by Figure 35, where PRC optimal body rate trajectories for the points in Figure 32 (c) with $z = 0.6$ and $z = 0.7$ are plotted.

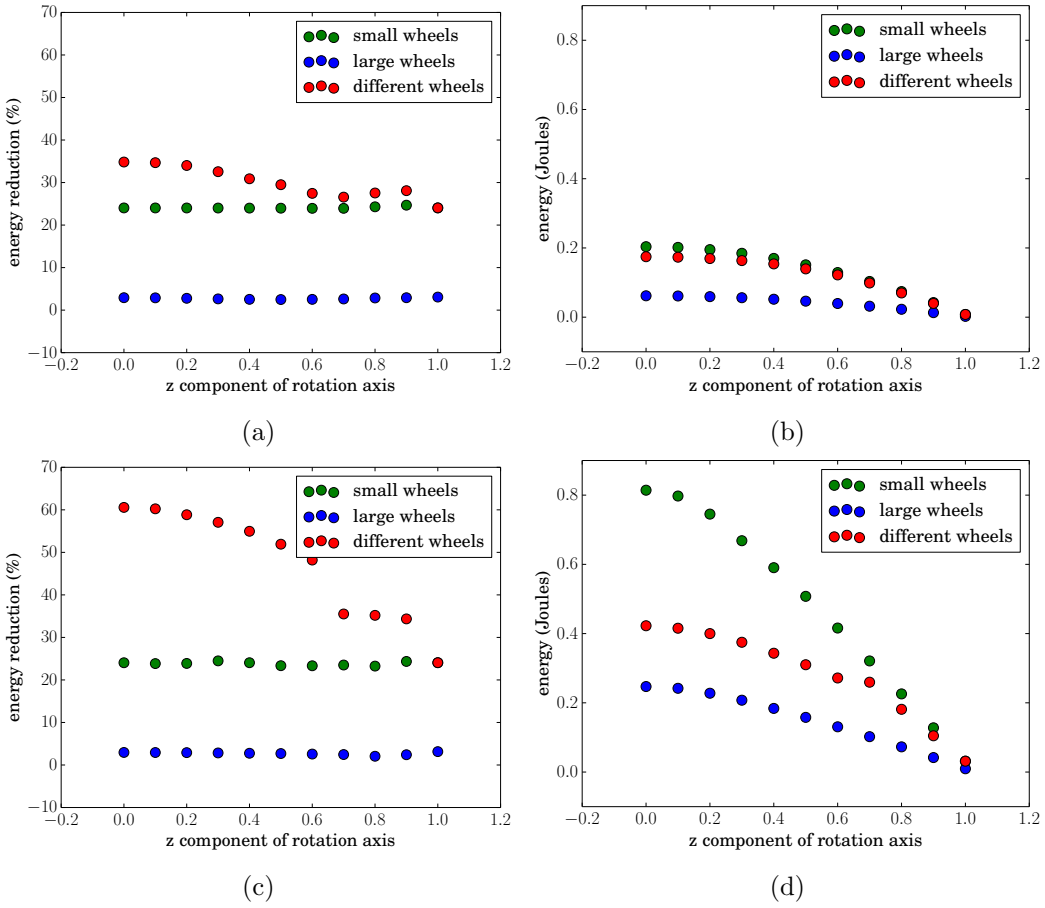

Figure 34: Variation of z component of rotation axis for three reaction wheel configurations. Wheel MOI are (in $kg \cdot m^2 \times 10^{-5}$): different wheels = [10 1 1], small wheels = [1 1 1], large wheels = [10 10 10]. (a) Percent energy reduction of PRC over TRC solutions, $\theta = \frac{\pi}{2}$. (b) Energy consumption of PRC optimal solutions, $\theta = \frac{\pi}{2}$. (c) Percent energy reduction of PRC over TRC solutions, $\theta = \pi$. (d) Energy consumption of PRC optimal solutions, $\theta = \pi$.

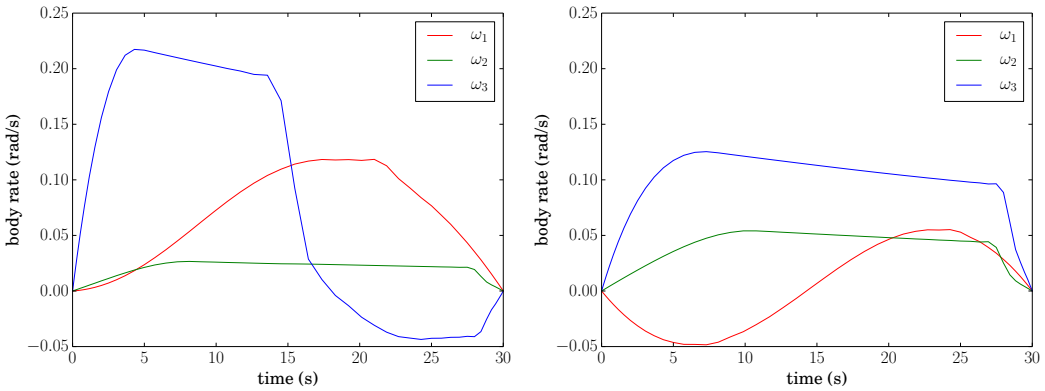

(a) (b)

Figure 35: PRC optimal body rate trajectories with $\theta = \pi$. (a) $z = 0.6$. (b) $z = 0.7$.

In Figure 34 (a) and (c), the energy reduction for different wheels decreases with increasing z, but is always greater than that of the small wheels (except when $z = 1$). However, in all of the maneuvers presented in this section, the x axis component of the rotation vector is 0. This makes for somewhat simpler trajectories, and provides a good illustration of the maximum extent of energy reduction that can be achieved using the PRC with differently sized wheels. For rotations with significant x axis components, the extent of the improvement will be significantly lower, closer to that afforded by the large wheel configuration. However, these maneuvers will be inexpensive anyways because of the large MOI of the x axis reaction wheel. For the most expensive maneuvers, with a large angle and large y axis component, the advantage of using the PRC over the TRC is significant.

5.5 Large Grids

In Chapter 3 the possibility of rapidly computing near optimal trajectories by interpolating from a precomputed grid of solutions was discussed. In this section, these grids are computed for several reaction wheel size configurations, and statistics are computed to compare the performance of the different running costs and reaction wheel configurations over a large number of final attitudes. The PRC and TRC are also compared to the eigenaxis maneuver. To facilitate this comparison, energy

consumption values are computed by simulating feedback tracking of the computed trajectories using the feedback controller in Chapter 4. Though the dynamics use a quaternion attitude representation, the sample points were chosen so as to comprise a uniform grid in the standard [*yaw pitch roll*] euler angle attitude representation. In order to sample the entire space of attitude maneuvers, the yaw, pitch, and roll ranges are, respectively: $[-\pi, \pi]$, $[-\frac{\pi}{2}, \frac{\pi}{2}]$, and $[-\pi, \pi]$. These are discretized with a resolution of $\frac{\pi}{10}$, so that there are 21 sample points in yaw, 11 in pitch, and 21 in roll, resulting in a three dimensional grid of $21 \times 11 \times 21 = 4851$ points. The maneuver time is $30s$ for all maneuvers presented in this section. Four configurations of reaction wheels are used, with the following values of MOI about their rotational axes (in $kg \cdot m^2 \times 10^{-5}$): small wheels [1 1 1], medium wheels [2.2 2.2 2.2], large wheels [10 10 10], and differently sized wheels [10 1 1].

The resulting distributions of energy consumption and energy reduction are presented in Figures 36 and 37, and summarized in Tables 2 and 3. In the case of uniform wheel sizes, energy reduction of PRC over TRC remained fairly constant across all maneuvers, so the averages presented in Table 3 for the uniform wheel size configuration are quite close to the improvements computed for a single final attitude in Figure 19. Improvements of the PRC and TRC over eigenaxis maneuvers are more variable. This is explained by fact that the eigenaxis maneuver does not take into account the dynamics of the satellite, so for some final attitudes the eigenaxis path happens to be closer to the optimal path than for others. For example, when the eigenaxis is aligned with the axis of rotation of one of the reaction wheels, the paths taken by the optimal solutions and eigenaxis solution are likely to be nearly the same. In this case, the difference between the trajectories would lie only in the acceleration profile. On the other hand, the paths taken by the TRC and PRC optimal trajectories always tends to be quite similar, with most of the difference in energy consumption being accounted for by differing acceleration profiles. This explains the consistency of improvement of the PRC over the TRC. For the differently sized wheels, the PRC over TRC energy reduction ranges between about 5 % and 60 %. The origins of this deviation were discussed in the previous section. The

distribution of TRC over eigenaxis energy reduction has about the same spread as that for the uniform reaction wheel size case.

Wheel Configuration	Eigen	TRC	PRC
small wheels	0.578 , 0.344	0.354 , 0.217	0.261 , 0.159
medium wheels	0.294 , 0.175	0.173 , 0.106	0.142 , 0.086
large wheels	0.128 , 0.076	0.090 , 0.055	0.090 , 0.054
different wheels	0.353 , 0.271	0.225 , 0.170	0.132 , 0.073

Table 2: Mean energy consumption (Joules) , standard deviation of energy consumption (Joules) over a large grid of final attitudes for four reaction wheel configurations.

Wheel Configuration	PRC over TRC	PRC over Eigen	TRC over Eigen
small wheels	26.15 , 1.46	54.86 , 2.87	38.79 , 4.89
medium wheels	18.17 , 1.29	51.77, 3.05	41.00 , 4.52
large wheels	0.25 , 1.04	29.63 , 4.92	29.45 , 4.94
different wheels	33.59 , 14.64	56.63 , 11.84	35.19 , 5.26

Table 3: Mean energy reduction (Percent) , standard deviation of energy reduction (Percent) achieved by using one trajectory computation approach over another, for four reaction wheel configurations.

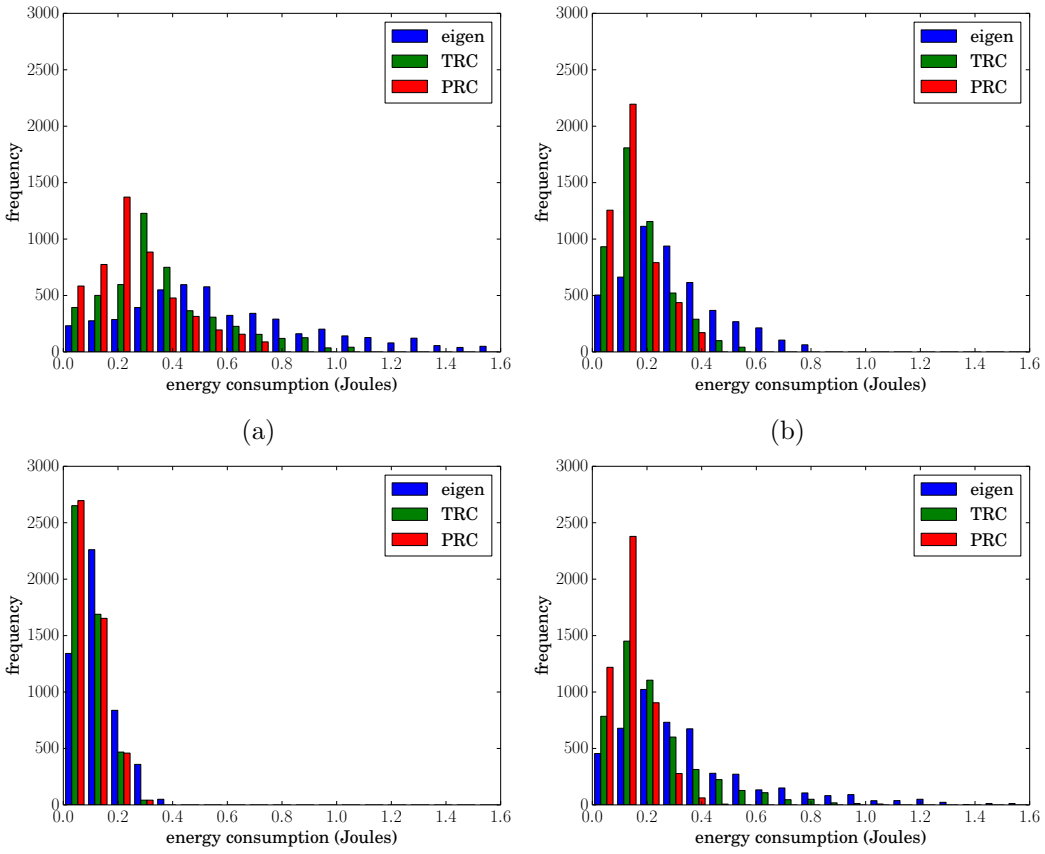

Figure 36: Distribution of energy consumption of maneuvers over final attitude grid for eigenaxis, TRC, and PRC trajectories, for four reaction wheel configurations. (a) Small wheels. (b) Medium wheels. (c) Large wheels. (d) Different wheels.

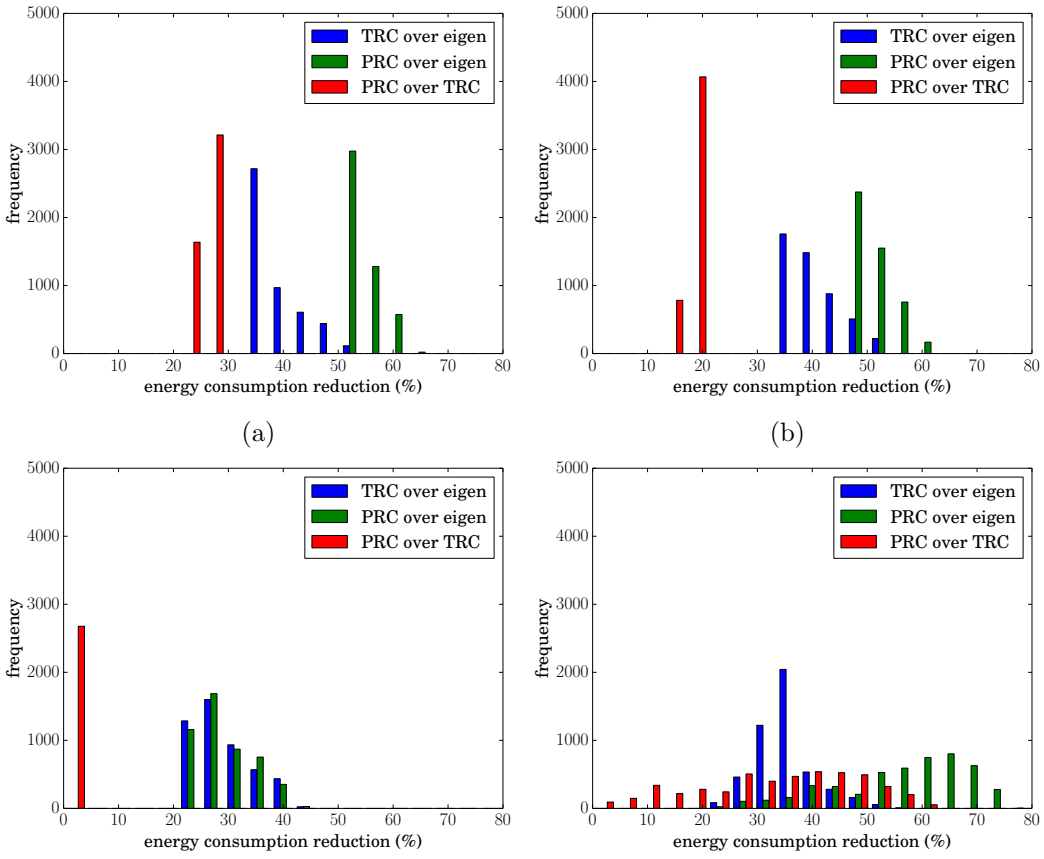

Figure 37: Distribution of energy consumption reduction achieved by using one trajectory computation approach over another, for four reaction wheel configurations. (a) Small wheels. (b) Medium wheels. (c) Large wheels. (d) Different wheels.

5.6 Summary

The energy consumption of maneuvers is inversely proportional to reaction wheel size. The energy reduction achieved using the PRC over the TRC becomes small either as the wheel size gets so small that the final time of the maneuver approaches the minimum time, or as the reaction wheels get so large that they do not have to spin quickly, and the energy dissipated in the armature resistance due to torque producing current dominates the cost. As reaction wheel size decreases, the TRC optimal control torque trajectories remain the same, until the point where reaction wheel speed saturation occurs and the trajectory changes radically. The PRC optimal control changes gradually, even as speed saturation occurs.

Energy consumption is also inversely proportional to maneuver time. Energy reduction achieved using the PRC over the TRC is reduced to zero as the time approaches the minimum feasible time and both solutions converge to the minimum time solution. For long times, the improvement is also reduced, since the maximum wheel speed during a maneuver gets small, and unrecoverable mechanical energy becomes insignificant. If the independent variable is normalized, the TRC optimal control torque trajectories for varying final times are related through t_f^{-2}, as long as the actuators don't saturate. This means that if a TRC optimal solution is known for one maneuver time, the optimal solution for any other non-saturating maneuver time can be trivially computed.

Though the energy consumption increases with increasing maneuver angle, the energy reduction of the PRC over the TRC remains nearly constant. Variation of the magnitude of the z component of the rotation axis also has a large impact on energy consumption, since the body MOI about the z-axis is approximately 5 times smaller than that about the x and y axes, but the PRC over TRC energy reduction remains fairly constant. The observed insensitivity of energy reduction to rotation angle and rotation axis suggest that the reduction was relatively independent of final attitude, a fact that was confirmed through the computation of large grids of solutions. These grids also showed significant energy reduction achieved with both optimal methods over the constant acceleration eigenaxis maneuver, though the degree of the reduction was more highly dependent on the final attitude.

Finally, the PRC is better able to exploit non-uniformity in the reaction wheel MOI than the TRC, since the TRC is indifferent to reaction wheel size because it does not contain any wheel speed terms. For the examined configuration, the maximum energy reduction was over 50%, but was highly dependent on the final attitude. Fortunately, the attitudes that required the highest energy consumption also produced the highest energy reduction in PRC over TRC optimal solutions.

6 Hardware Implementation

The work presented in previous chapters performed optimization based on a power model which included three loss sources: resistive losses in the motor armature, frictional losses, and mechanical energy which cannot be recaptured when a regenerative braking system is lacking. The availability of a high performance motor driver with negligible losses was assumed. In order to evaluate the performance of the optimal solutions with a real world driver, a BLDC driver board was built. The driver losses incurred by this board proved to be non-negligible, and, for the evaluated trajectory, both the TRC and eigenaxis maneuvers outperformed the PRC. For all trajectories, energy consumption was significantly higher than that which was predicted. In order to explain this discrepancy, several driver loss sources were evaluated, and the primary culprit was identified as inaccuracy in the rotor position estimate. Though the test was not successful, it motivated the evaluation of conditions on the motor driver that must be met in order for this kind of trajectory optimization to be valuable. It was also observed that power consumption was proportional to the magnitude of reaction wheel velocity with a low performance commutation algorithm, suggesting that trajectory optimization of a running cost equal to the absolute value of the reaction wheel velocity would be valuable if such an algorithm were used.

6.1 Experimental Set Up

A momentum wheel with a MOI of approximately $1 \times 10^{-5} kg \cdot m^2$ was attached to the rotor of a Faulhaber 2010 012b BLDC motor [3] which was affixed to a tabletop. The motor was driven using a Texas Instruments DRV8312 integrated brushless motor driver [33]. Control signals to the driver were generated by a dsPIC33 microcontroller [25]. The microcontroller uses signals from the motor's integrated Hall effect sensors to drive a rotor position and speed estimator and uses these estimates to implement speed control and commutation. The commutation algorithm used was space vector modulation (SVM) [24], the only motor quantity measured by the controller being

the state of the Hall effect sensors. The microcontroller is connected to a PC through a UART serial connection.

The motor is powered by a DC power supply, so, unlike a battery, no voltage sag occurs with current draw. Current is measured by amplification of the voltage differential created across a 1Ω shunt resistor. All logic is powered by a separate supply, so the current measured is only that which flows through the drive electronics and into the motor. The current amplifier is one sided, meaning only current flowing out of the supply is measured, which is acceptable since it is assumed that the satellite power system does not accept reverse current flow. To check if this was the case with the experimental set up, the polarity of the amplifier was reversed, but no current was observed flowing into the supply, confirming that the non-regenerative braking assumption was valid in the given set up. The amplified signal is converted to a digital signal by an ADC (Analog to Digital Converter) and reported to the PC via serial stream. In order to minimize the effect of noise generated by the switching electronics the amplifier and ADC were on a separate board from the motor driver, and used a different power supply.

The reaction wheel speed trajectory is known for the computed optimal solutions, and can be obtained for the eigenaxis trajectory through simulation of feedback control. The PC then communicates this trajectory to the microcontroller in real time with a frequency of 10Hz, and the microcontroller uses these inputs as commands to the speed controller. Measured reaction wheel speeds and current consumption are reported back to the PC at a rate of 10Hz. Power consumption is evaluated by multiplying the measured current by the supply voltage.

6.2 Commutation

The space vector modulation algorithm is more difficult to implement and requires greater computational resources than block commutation, but can theoretically implement maximally efficient control if good estimates of relevant motor quantities

are available. [24] offers an excellent overview of PMSM motor control techniques. In brief, the goal of PMSM motor control is to generate the appropriate voltages on each of the motor's three phases such that the magnetic field produced by the armature coils is 90° electrical ahead of that of the rotor, so as to produce the maximum amount of torque for a given current, and eliminate torque ripple. To do so requires precise knowledge of the orientation of the rotor at all times. Rotary encoders are often used to obtain this information. However, the test setup only had hall effect sensors, not an encoder. Thus, a Kalman filter based on Hall effect sensor measurements was implemented to estimate the rotor position.

Hall effect sensors provide an absolute position measurement with a resolution of 60° electrical. However, the position is known relatively precisely when the Hall effect sensor state transitions. Velocity is estimated by measuring the time between Hall effect sensor transitions. With the velocity known, the rotor angle can be extrapolated from the precisely known transition orientation. Since the dynamics of the reaction wheel are simple, this approach works relatively well. However, there is a non-negligible amount of noise in the velocity measurements that can arise from imperfect placement of Hall effect sensors and delays in transition time latching. Furthermore, this method produces errors when the motor is accelerating. Attempts to account for acceleration in the estimator failed to improve performance. The estimator also performs poorly at low speeds when transitions between Hall effect sensors are infrequent.

6.3 Speed Control

In order to maintain comparability to the simulation, the speed controller that was implemented was similar to that described in Chapter 4, where the speed error is multiplied by a constant to produce the commanded torque. The torque produced by the motor (τ) can be approximated by:

$$\tau = k_t * \frac{(V_o - V_m)}{R} \tag{48}$$

where k_t is the motor torque constant, $V_o = V_b \times DC$ is the average voltage output of the driver which is equal to the battery voltage times the switching duty cycle, V_m is the back EMF, and R is the armature resistance. The back EMF is computed by multiplying the rotor speed estimate by the motor electrical constant, and V_o is set to produce the desired torque. This approach produces a non-zero steady state error due to errors in the estimates of velocity and electrical constant.

6.4 Experimental Results

Since the estimator performs poorly at low wheel speeds, a final attitude which produced optimal trajectories with high reaction wheel speeds was chosen. Maneuvering to this attitude does not require the z axis wheel to rotate in any of the three trajectory computation approaches (which is convenient because the z axis wheel tends to rotate much more slowly than the others due to the low satellite body MOI about the z axis). Resultant power and velocity trajectories, as well as those predicted by simulation, are presented in Figures 38, 39, and 40. Energy consumed by the three maneuvers is summarized in Table 4.

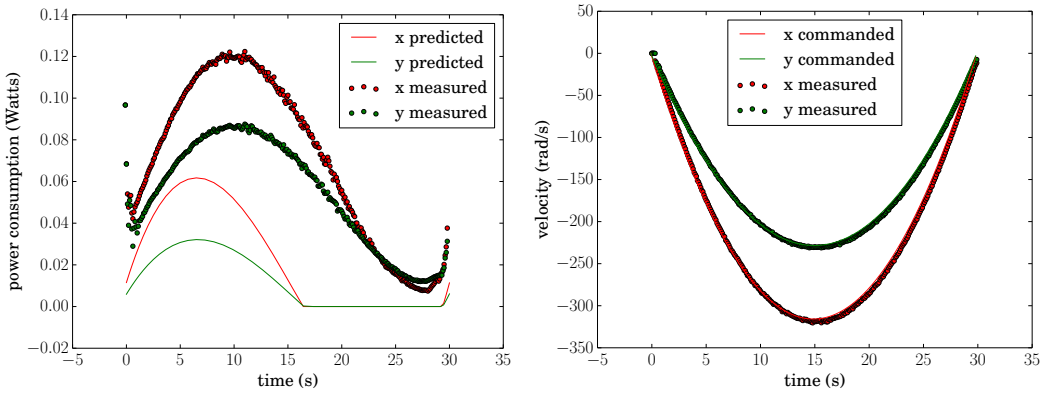

(a) (b)

Figure 38: Theoretical and experimental trajectories for TRC optimal solution, for x and y axis reaction wheels. (a) Power consumption. (b) Reaction wheel speed.

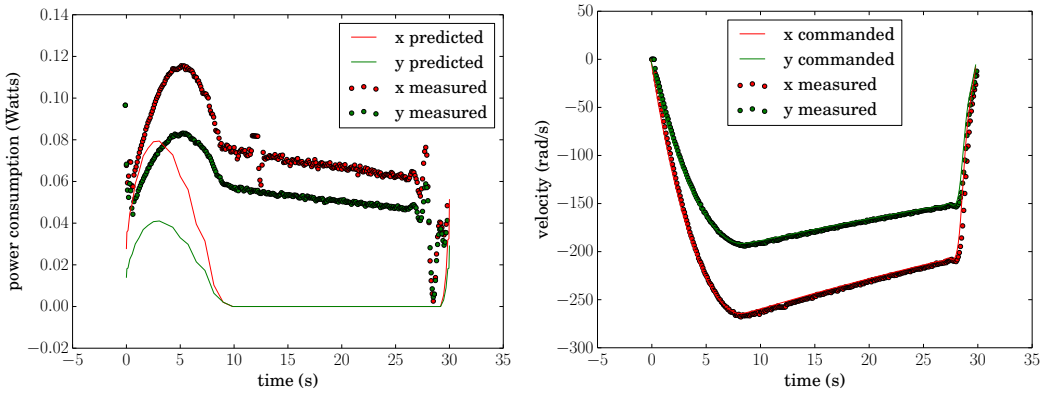

(a) (b)

Figure 39: Theoretical and experimental trajectories for PRC optimal solution, for x and y axis reaction wheels. (a) Power consumption. (b) Reaction wheel speed.

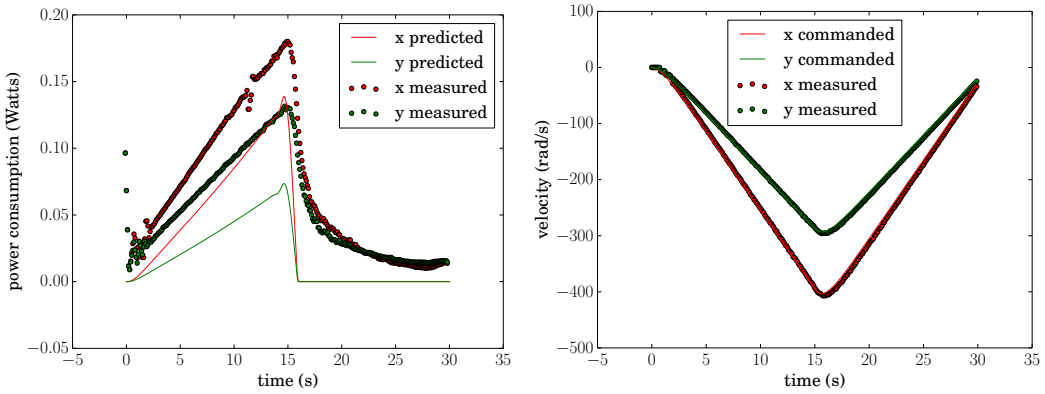

(a) (b)

Figure 40: Theoretical and experimental trajectories for eigenaxis maneuver, for x and y axis reaction wheels. (a) Power consumption. (b) Reaction wheel speed.

eigen	TRC	PRC
3.64	3.73	3.91

Table 4: Total energy consumed by maneuvers during experiment (Joules).

In all cases, there are significant discrepancies between the simulated and experimental power trajectories, the experimental trajectories consuming more energy in all cases. These additional losses were enough to make the absence of regenerative braking irrelevant, since the power consumed by the motor was always greater than zero. As a result of the significant unmodeled losses, the eigenaxis trajectory performed best, followed by the TRC, and the PRC optimal solution performed worst.

In the following section, some of the potential sources of these losses are accounted for.

6.5 Potential Loss Sources

There are a variety of potential loss sources that could explain the discrepancy between the measured and predicted power trajectories. One potentially significant loss source can result from increased current ripple if the switching frequency is not high enough compared to the RL time constant of the motor windings. The value of this time constant, τ, was $69\mu s$, and the switching period was $14\mu s$. At this switching rate, these losses are fairly insignificant (Figure 41(a)), though they can become severe if the switching frequency is too low, as is the case in Figure 41(b). The ripple losses, while not negligible, are not sufficient to explain the discrepancy between the experimental and simulated power trajectories. Refer to Appendix B for the method used to compute these losses.

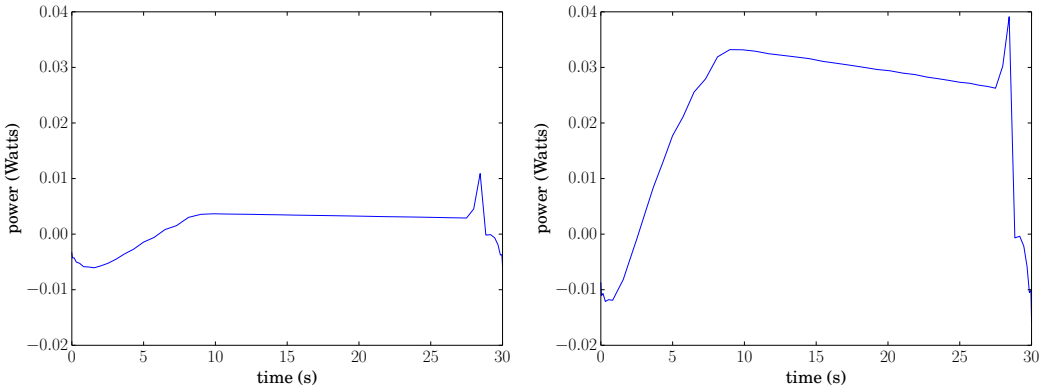

(a) (b)

Figure 41: Ripple losses arising from insufficient switching frequency. (a) 70 kHz. (b) 70/4 kHz.

Another potential source of power loss is known as switching loss, which occurs during the linear transition region between the MOSFET's on and off states. An expression for these losses, broken down by high side losses (P_{switch}^{HS}) and low side

losses (P^{HS}_{switch}), is given in [26]:

$$P^{HS}_{switch} = \frac{1}{2} \times V_b \times I_b \times t_R \times f_{sw} \tag{49}$$

$$P^{LS}_{switch} = \frac{1}{2} \times V_b \times I_b \times t_F \times f_{sw} \tag{50}$$

$$P_{switch} = P^{HS}_{switch} + P^{LS}_{switch} \tag{51}$$

where t_R and t_F are the output rise and fall times, respectively, and f_{sw} is the switching frequency. The rise and fall times depend on the load. With a resistive load, these are both quoted as $14ns$ in the motor driver datasheet [33], though with an inductive load they may be higher. f_{sw} in the experimental setup is 70 kHz, so, using the quoted rise and fall times, $t_R \times f_{sw} = t_F \times f_{sw} = 0.00098$, meaning these losses are negligible. Conduction losses, due to the effective resistance of a fully turned on switch, are also insignificant, as the MOSFETs' turned on resistance ($80m\Omega$) is two orders of magnitude lower than that of the coil windings.

Even when the motor was stationary and no torque is applied (or when the motor was disconnected), a significant amount of current consumption was observed when the driver was enabled. These losses, hereafter referred to as basic losses, proved to be dependent on the switching frequency and the duty cycle, and are likely the result of the combined effect of gate drive losses, shoot through, and output capacitive losses, since these are independent of load current [17]. These losses were characterized by setting the same duty cycle on all three phases so that no current was made to flow through the motor, and then measuring the current consumed by the driver. The effects of varying the duty cycle on the basic losses are presented in Figure 42. Because basic losses drop to zero for both 0% and 100% duty cycles, it is clear that they are rooted in the switching action of the driver. These losses are significant, as evident from Figure 42, and are estimated to account for approximately 1/4 of energy consumption.

We believe that the majority of the added cost of the experimental trajectories stems from error in the rotor orientation estimate. If the stator field is not optimally

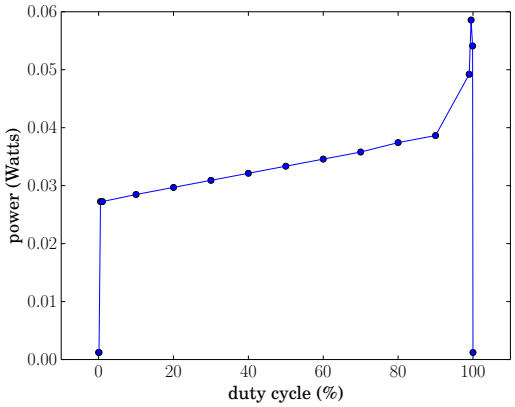

Figure 42: Power consumed by basic losses as duty cycle is varied.

aligned, a greater current is needed to produce the necessary acceleration. Even maintaining a constant velocity, which should not consume any current except that needed to overcome frictional losses, incurs a cost with an erroneous estimator, since the voltage output by the driver is out of phase with the back EMF. Thus, even though the magnitude of both may be nearly equal, current will still flow through the coils.

Furthermore, at high rotor speeds, the output voltage must be updated rapidly to keep up with the rotor angle. However, since each update requires an update of the estimator, the SVM output refresh rate is limited by the computational facilities of the microcontroller. In the experimental setup, the estimator/SVM update loop was run at 6500 Hz, which was probably sufficient for the maximum speeds achieved during the experiment (about 400 rad/s). Running at this rate on the given hardware required a fixed point implementation, which may have introduced some numerical errors.

In order to demonstrate how significant the losses produced by estimation error can be, a trajectory was executed where the SVM modulation scheme was implemented without extrapolating the rotor orientation between Hall effect transitions (Figure 43), a control scheme which is similar to block commutation. The power consumption increases by an order of magnitude, and based on the shape of the curve it is clear that the dominant loss is linearly proportional to the magnitude of the reaction

wheel velocity.

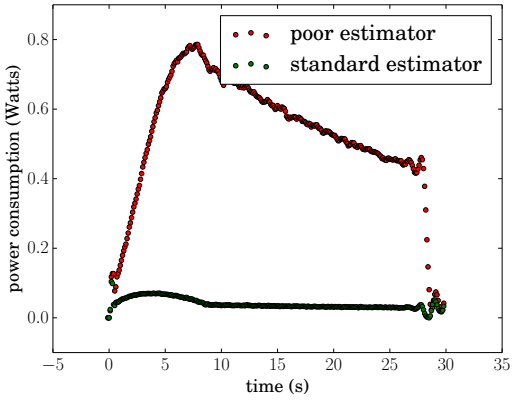

Figure 43: Power curves for a single motor trajectory executed both the extrapolating and non-extrapolating commutation methods.

6.6 Lessons Learned

The failed attempt at validation of the simulation results demonstrated that an efficient motor driver and algorithm are necessary for TRC and PRC optimization to be valuable. On the other hand, if a very inefficient commutation algorithm, such as block commutation, is used, trajectories which minimize the integral of the velocity magnitude may provide significant cost savings. A designer attempting to minimize the energy consumption of the RWA should first focus on the driver and driver algorithm, and perform trajectory optimization once a sufficient level of driver efficiency is achieved.

The use of a rotary encoder for estimating rotor position is recommended, since it gives precise positional information without any significant computational overhead. In fact, some microcontrollers have a dedicated quadrature encoder interface to facilitate simple, efficient estimation. Though extrapolation between Hall effect sensor transitions can significantly reduce energy consumption compared to block commutation, encoders would allow for more efficient control with lower computational overhead. Appropriate sizing of the driver is also critical. The driver used in the experiment was capable of driving much higher currents than necessary. If

the driver were optimized for the given motor, losses could be reduced through the use of smaller MOSFETs. Attention should also be given to minimizing the capacitance on the driver output, since capacitive losses can be a major component of the basic loss. Finally, the microcontroller and MOSFETs should be chosen such that they can support a switching period that is at least 5 times shorter than the LR time constant of the motor windings, otherwise current ripple losses start to become significant.

7 Conclusions and Future Work

7.1 Conclusions

In the pursuit of minimizing the energy consumed by reaction wheel array maneuvers, a tradeoff exists between efficiency and ease of implementation. The easiest approach is to constrain rotation to the eigenaxis and choose a reasonable velocity profile, an approach that is so computationally inexpensive that these maneuvers can be computed in flight on the lowest performance microcontrollers. The energy efficiency of this approach depends on the maneuver angle and MOI of the satellite body, since dynamics are not taken into account. Direct pseudospectral optimal control methods account for the satellite dynamics and can therefore produce much more efficient maneuvers. Furthermore, these methods can be used to achieve shorter maneuver times since the path is not constrained to the eigenaxis. Unfortunately, the time required to compute the optimal solution can be substantial, even on sophisticated hardware, which presents some implementation challenges. Maneuvers can be computed on the ground and communicated to the satellite via radio at execution time, but this reduces the satellite's potential for autonomy and increases strain on the communication system and the ground station. This work demonstrated an approach for the rapid computation of solutions for arbitrary final attitudes in orbit based on interpolation from a bank of precomputed solutions, and it was shown that the energy costs of solutions computed by interpolation were nearly identical

to those computed directly.

When performing trajectory optimization, a simple, convenient choice of running cost is the sum of squares of the control torques, denoted TRC, because this quadratic running cost is smooth and convex, and therefore well suited to numerical optimization. Furthermore, computation of this running cost does not involve any modeling of losses, or knowledge of motor parameters. Additionally, extrapolation of TRC optimal solutions to varying maneuver times was shown to be trivial as long as the actuators did not saturate. However, not all RWA energy losses are proportional to the sum of squares of control torque, so better performance can be achieved by modeling these losses.

The power running cost (PRC) was formulated to account for some of these losses, namely, resitive losses in the stator armature, frictional losses in the bearings, and mechanical energy that is unrecoverable in the absence of a regenerative braking system. Modeling the lack of regenerative braking created a discontinuity in the derivative of the running cost at zero, which made it impossible for the optimal control solver to find a solution. To remedy this issue, the running cost was approximated by a hyperbolic function with a tuning parameter that traded off accuracy and computational burden. A solution very close to the true optimal could be attained by computing a series of solutions to increasingly more accurate approximations, using the solution to one problem as the initial guess for the next. This method was inefficient, because it required many runs of the solver to obtain a single solution. A different approach, which involved the addition of variables and reformulation of the nonsmoothness of the running cost as a path constraint, proved much more efficient and did not require approximation.

In practical implementations of optimal attitude maneuvers, the optimal quaternion trajectories are used as input to a feedback tracking controller. The effects of the feedback gains of the controller on energy consumption and final attitude error were evaluated, and it was shown that as the feedback gains get large, the energy consumption of the simulated feedback trajectory matches that of the optimal solution,

while for smaller gains energy consumption is lower, but there is an error in the final attitude. This analysis assumed the availability of a perfect estimator and controller, but in reality the feedback gains would be limited by the noise on these devices. It was also demonstrated, through simulation, that small errors (up to 10%) in the body MOI estimate did not have a significant effect on maneuver efficiency.

The effects of variations in reaction wheel size, maneuver time, and final orientation on energy consumption and the energy reduction attained using the PRC over the TRC were evaluated extensively. Energy consumption increases with: a) decreasing reaction wheel MOI, b) decreasing maneuver time, c) increasing maneuver angle. Since the MOI of the satellite body was much lower about the z axis than the x and y axes, it was also shown that the greater the z component of the eigenaxis, the lower the maneuver cost. Energy reduction of PRC over TRC optimal solutions was highly dependent on reaction wheel MOI and maneuver time, but relatively independent of final orientation (as long as actuator saturation was avoided). The smaller the reaction wheel, the faster it has to spin to produce the desired angular velocity in the satellite body. Increased spin rates lead to greater unrecoverable kinetic energy and frictional losses, so for smaller reaction wheels the PRC, which accounts for these losses, yielded significantly more efficient results. For long maneuver times, the difference between solutions produced by the two running costs is not significant, since maneuvers become very energetically inexpensive. As maneuver time approaches the minimum possible for the given reaction wheel size and final attitude, both PRC and TRC optimal solutions approach the minimum time solution, and incur similar energy costs. In this scenario, the only way to meet the constraints is to expend large quantities of energy.

Execution of optimal wheel speed trajectories with a real motor highlighted the fact that for the optimization methods described in this work to be useful, a highly efficient motor driver is necessary as the losses due to imperfect motor control and inefficient electronics can outweigh those considered in this work. An efficient driver must be capable of making accurate rotor position measurements and switching with

a period that is an order of magnitude lower than the RL time constant of the motor. Appropriate MOSFET sizing and a printed circuit board designed to minimize output capacitance are also important for driver efficiency. If an unsophisticated control algorithm such as block commutation is used, power consumption will be much higher and proportional to motor speed magnitude. In this case, energy consumption is linearly inversely proportional to reaction wheel MOI, and could be minimized through trajectory optimization with respect to the magnitude of the velocities of the reaction wheels.

7.2 Future Work

Chapter 6 demonstrated that a highly efficient driver is necessary for optimization with respect to the PRC to be valuable. In general, driver efficiency is something that RWA designers should be concerned with. On the other hand, the natural continuation of this thesis would be to account for driver losses in the running cost. This would increase the value of trajectory optimization for systems with inefficient motor drivers, which are possibly the ones that have the most to gain from maneuver optimization. A method to determine driver losses of an RWA experimentally should be developed, so that they can be accurately modeled by the running cost. Accurate modeling of driver losses may also require the incorporation of the feedback controller dynamics into the dynamic constraints.

If the interpolation scheme is used to increase satellite autonomy, some flexibility in the types of optimal maneuver that can be performed is lost. A method for extrapolating PRC maneuvers to different maneuver times should be developed, so that a separate grid of solutions does not have to be computed for each desired maneuver time. However, there are a number of other conditions that may change. It may be desireable to execute maneuvers with non-zero initial wheels speeds, visit multiple waypoints in a single maneuver, or restrain the attitude from entering certain forbidden zones (in order to keep sensitive instruments pointed away from the sun, for example). Precomputation of solutions that cover all possible maneuvers is

not feasible. Therefore, achieving this level of flexibility while maintaining autonomy would require solutions to be computed on-board the satellite. If great care was paid to problem formulation and scaling, and if FPGA (Field Programmable Gate Array) technology was leveraged to allow for highly customizable computational logic, then it may be possible to create a computer capable of solving the optimal energy attitude control problem in a reasonable amount of time aboard a small satellite. This would be an interesting and useful direction for future research.

Finally, field testing of the results presented in this work is critical. In the same way as the work done in Chapter 6 revealed the importance of consideration of driver losses, field testing could reveal additional effects that are significant and require consideration. Testing on a spherical air bearing may be a reasonable first step. However, air bearing test beds tend to have much larger MOIs than the actual satellites, and the removal of gravitational torques by mass balancing is challenging. The best way to test the results of the simulation would be in orbit. The launch of a conventional, full scale satellite to verify the results of a Master's thesis is hard to imagine, but, with a Cubesat, it might just be possible.

8 Appendices

A Derivation of 1D TRC Optimal Solution

The one dimensional equivalent of the dynamics can be formulated as:

$$\begin{bmatrix} \dot{\theta} \\ \ddot{\theta} \end{bmatrix} = \begin{bmatrix} 0 & 1 \\ 0 & 0 \end{bmatrix} \begin{bmatrix} \theta \\ \dot{\theta} \end{bmatrix} + \begin{bmatrix} 0 \\ I^{-1} \end{bmatrix} u \tag{52}$$

Where θ is the orientation angle, u is the torque exerted by the control system on the satellite, and I is the MOI of the satellite body. For the remainder of this derivation, we set $I = 1$ for notational simplicity. Since the TRC does not include the reaction wheel speed, the reaction wheel dynamics needn't be modeled, and it is assumed that no state or control saturation limits are reached.

An analytical solution is obtained through the application of Pontryagin's principle. Notation is adopted from [29]. First, the Hamiltonian (H) is formulated as:

$$H = u^2 + \lambda_1 \dot{\theta} + \lambda_2 u \tag{53}$$

where λ_1 and λ_2 are the costates corresponding to θ and $\dot{\theta}$, respectively. The endpoint constraints are used to formulate the endpoint Lagrangian ($\bar{E}$) as follows:

$$\bar{E} = \nu_1(\theta_0 - 0) + \nu_2(\theta_f - \theta^f) + \nu_3(\dot{\theta}(t_0) - 0) + \nu_4(\dot{\theta}_f - 0) + \nu_5(t_0 - 0) + \nu_6(t_f - t^f) \tag{54}$$

where a subscript of 0 or f indicates the initial or final value of a variable, a superscript indicates the initial or final value of a variable required by a constraint, and ν_1 through ν_6 are endpoint Lagrange multipliers. Application of the Hamiltonian

minimization, value, and evolution conditions yields, respectively:

$$u = \frac{-\lambda_2}{2} \tag{55}$$

$$H_f = -\nu_6 \tag{56}$$

$$\dot{H} = 0 \tag{57}$$

The differential Eq.s governing the costates are obtained by differentiating H with respect to the states:

$$\dot{\lambda_1} = 0 \tag{58}$$

$$\dot{\lambda_2} = -\lambda_1 \tag{59}$$

Combing Eq.s 55 and 53:

$$H = \lambda_1 \dot{\theta} - \frac{\lambda_2^2}{4} \tag{60}$$

Evaluating Eq. 60 at t_f, recognizing that $\dot{\theta}_f = 0$, and combining with Eq. 56:

$$\nu_6 = \frac{\lambda_{2,f}^2}{4} \tag{61}$$

Since the Hamiltonian is constant(Eq. 57), combining Eq.s 60 and 61:

$$\lambda_1 \dot{\theta} - \frac{\lambda_2^2}{4} = -\frac{\lambda_{2,f}^2}{4} \tag{62}$$

Evaluating Eq. 62 at t_0, and recognizing that $\dot{\theta}_0 = 0$:

$$\lambda_{2,0}^2 = \lambda_{2,f}^2 \tag{63}$$

$$\lambda_{2,0} = \pm\lambda_{2,f} \tag{64}$$

From Eq.s 58 and 59 it is known that the derivative of λ_2 is constant. If $\lambda_{2,0} = \lambda_{2,f}$, then λ_2, and therefore u, must be constant. This is impossible since the initial and final velocities are zero, but $\theta_f - \theta_0 \neq 0$. Therefore, it must be that $\lambda_{2,0} = -\lambda_{2,f}$.

From this, and the fact that the derivative of λ_2 is constant:

$$\lambda_2 = \lambda_{2,0} - 2\frac{\lambda_{2,0}}{t_f}t \tag{65}$$

Combining with Eq. 55:

$$u = \lambda_{2,0}(\frac{1}{t_f}t - \frac{1}{2}) \tag{66}$$

Integrating Eq. 66 twice with respect to time from t_0 to t_f gives θ_f, since $\theta_0 = 0$.

$$\theta_f = -\frac{1}{12}\lambda_{2,0}t_f^2 \tag{67}$$

$$\lambda_{2,0} = -12\frac{\theta_f}{t_f^2} \tag{68}$$

Finally, combining Eq.s 66 and 68 gives the closed form solution for the optimal control as a function of the desired angle and maneuver time:

$$u = -12\frac{\theta_f}{t_f^2}(\frac{t}{t_f} - \frac{1}{2}) \tag{69}$$

B Accounting for Ripple Losses

The single phase equivalent circuit for the three phase PMSM motor and driver is shown below. The MOSFETs are modeled as switches. R and L are the resistance and inductance of the motor, and equal to 3/4 of their respective phase to phase quantities. The voltage supplied to the motor, V_p, is equal to V_b when the high side switch is closed and the low side open, and 0 when the opposite is true.

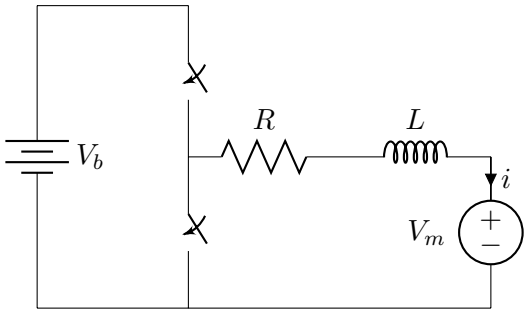

Figure 44: One phase equivalent circuit.

Circuit analysis gives the following first order differential Eq. for the current, i:

$$\frac{di}{dt} + \frac{R}{L} = k \tag{70}$$

$$k = \frac{2}{3}\frac{V_p - V_m}{R} \tag{71}$$

the solution to which is:

$$i = k(1 - e^{-t/\tau}) + i_0 e^{-t/\tau} \tag{72}$$

$$\tau = \frac{L}{R} \tag{73}$$

where i_0 is the current at $t = 0$. The energy dissipated by the resistance between $t = 0$ and $t = t_f$ is:

$$\begin{aligned}\int_0^{t_f} Ri^2\, dt = k^2[t_f + 2\tau(e^{-t_f/\tau} - 1) + \frac{\tau}{2}(1 - e^{-2t_f/\tau})] + \\ ki_0\tau[2(1 - e^{-t_f/\tau}) + e^{-2t_f/\tau} - 1] + \\ i_0^2\frac{\tau}{2}[1 - e^{-2t_f/\tau}]\end{aligned} \tag{74}$$

assuming that k is constant. Given i_0, the switching period (t_p), the duty cycle (d), V_b, and V_m, Eq. 74 can be used to evaluate the energy consumed by a single switching cycle. Dividing this energy by the switching period yields the average power consumption during the cycle. Since the switching rate is much higher than

the mechanical time constant of the rotor, V_m is assumed to be constant, therefore the assumption that k is constant is satisfied, provided that the high and low phases of the switching cycle are analyzed separately.

V_m is obtained by multiplying the rotor speed by the motor's electrical constant. The average current during a switching cycle, i_{avg}, is obtained by dividing the control torque by the torque constant. d and i_0 are then chosen such that $i_0 = i_f$ (the current at the end of the switching cycle) and the average current during the cycle is equal to i_{avg}.

Having solved for the total power dissipated in the resistance, the ripple current losses are found by subtracting power consumption computed with some very small value of t_p from the total power consumption.

References

[1] HSL. A collection of Fortran codes for large scale scientific computation. http://www.hsl.rl.ac.uk.

[2] Micro Reaction Wheel. Technical report, Blue Canyon Technologies, Boulder, Colorado.

[3] Series 2610 ... B Datasheet. Technical report, Dr. Fritz Faulhaber GMBH & CO. KG, 2014.

[4] P.R. Amestoy, I.S. Duff, J. Koster, and J.-Y. L'Excellent. A fully asynchronous multifrontal solver using distributed dynamic scheduling. *SIAM Journal of Matrix Analysis and Applications*, 23(1):15–41, 2001.

[5] V.M. Becerra. *PSOPT Optimal Control Solver User Manual. Release 3*, 2010. Available: `http://code.google.com/p/psopt/downloads/list`".

[6] Nazareth S. Bedrossian, Sagar Bhatt, Wei Kang, and I. Michael Ross. Zero-propellant maneuver guidance. *IEEE Control Systems Magazine*, 29(5):53–73, 2009.

[7] J.T. Betts. *Practical Methods for Optimal Control and Estimation Using Nonlinear Programming*. Society for Industrial and Applied Mathematics, 2010.

[8] K.D. Bilimoria and B. Wei. Time-optimal three-axis reorientation of rigid spacecraft. *Journal of Guidance, Control, and Dynamics*, 16(3):446–452, 1993.

[9] Robin Blenden and Hanspeter Schaub. Regenerative Power-Optimal Reaction Wheel Attitude Control. *Journal of Guidance, Control, and Dynamics*, 35(4):1208–1217, 2012.

[10] Cal Poly SLO. Cubesat Design Specification (Rev 13), 2015.

[11] John L Crassidis, F. Landis Markley, and Yang Cheng. A Survey of Nonlinear Attitude Estimation Methods. *Journal of Guidance, Control, and Dynamics*, 30:12–28, 2007.

[12] Michael James Develle. *Optimal Attitude Control Management For A Cubesat*. Master's thesis, University of Central Florida, 2011.

[13] Andrew Fleming. *Real-Time Optimal Slew Maneuver Design and control*. Master's thesis, Naval Postgraduate School, 2004.

[14] Andrew Fleming, Pooya Sekhavat, and I Michael Ross. On The Minimum-Time Reorientation of a Rigid Body. In *AIAA Guidance, Navigation, and Control Conference*, Chicago, IL, 2009.

[15] E. Gill, P. Sundaramoorthy, J. Bouwmeester, B. Zandbergen, and R. Reinhard. Formation flying within a constellation of nano-satellites: The QB50 mission. *Acta Astronautica*, 82(1):110–117, 2013.

[16] Qi Gong, Fariba Fahroo, and I. Michael Ross. Spectral Algorithm for Pseudospectral Methods in Optimal Control. *Journal of Guidance, Control, and Dynamics*, 31(3):460–471, 2008.

[17] David Jauregui, Bo Wang, and Rengang Chen. Power Loss Calculation with Common Source Inductance consideration for Synchronous Buck Converters. *SLPA009-20011 Texas Instruments ...*, (July):17, 2011.

[18] Mark Karpenko, Sagar Bhatt, Nazareth Bedrossian, and I. Michael Ross. Flight Implementation of Shortest-Time Maneuvers for Imaging Satellites. *Journal of Guidance, Control, and Dynamics*, 37(4):1069–1079, 2014.

[19] Siddharth S Kedare. *Space Environment Modelling and Torque-Optimal Guidance for CubeSat Applications*. Master's thesis, Carleton University, 2014.

[20] Planet Labs. Planet Labs Home Page, 2016.

[21] Unsik Lee and Mehran Mesbahi. Quaternion Based Optimal Spacecraft Reorientation. *Advances in the Astronautical Sciences*, 150:1–16, 2014.

[22] Harleigh Marsh, Qi Gong, and Mark Karpenko. Minimum energy attitude control. Technical report, Naval Postgraduate School, 2015.

[23] Robert G. Melton. Hybrid methods for determining time-optimal, constrained spacecraft reorientation maneuvers. *Acta Astronautica*, 94(1):294–301, 2014.

[24] James Robert Mevey. *Sensorless Field Oriented Control of Brushless Permanent Magnet Synchronous Motors*. PhD thesis, Kansas State University, 2006.

[25] Microchip Technology. dsPIC33EPXXXGP50X, dsPIC33EPXXXMC20X/50X and PIC24EPXXXGP/MC20X - 16-Bit Microcontrollers and Digital Signal Controllers with High-Speed PWM, Op Amps and Advanced Analog, 2013.

[26] Peter Millett. SLVA504_Calculating Motor Driver Power Dissipation. (February):1–5, 2012.

[27] I Michael Ross and Fariba Fahroo. Legendre pseudospectral approximations of optimal control problems. *New Trends in Nonlinear Dynamics and Control and their Applications*, 295(January):327–342, 2003.

[28] I. Michael Ross and Mark Karpenko. A review of pseudospectral optimal control: From theory to flight. *Annual Reviews in Control*, 36(2):182–197, 2012.

[29] I.M. Ross. *A Primer on Pontryagin's Principle in Optimal Control.* Collegiate Publishers, 2 edition, 2015.

[30] Hanspeter Schaub. AIAA 2008-6259 Locally Power-Optimal Spacecraft Attitude Control for Redundant Reaction Wheel Cluster. In *AIAA/AAS Astrodynamics Specialist Conference*, Honolulu, Hawaii, 2008.

[31] Haijun Shen and Panagiotis Tsiotras. Time-Optimal Control of Axi-Symmetric Rigid Spacecraft. In *AIAA Guidance, Navigation, and Control Conference*, Boston, MA, 1998.

[32] Planetary Society. Planetary Society Web Page.

[33] Texas Instruments. DRV83x2 Three-Phase PWM Motor Driver, 2014.

[34] Andreas Wächter and Lorenz T. Biegler. On the implementation of primal-dual interior point filter line-search algorithm for large-scale nonlinear programming. *Mathematical Programming*, 106:25–57, 2006.

[35] A. Walther and A. Griewant. Getting started with adol-c. In U. Naumann and O.Schenk, editors, *Combinatorial Scientific Computing*, pages 181–202. Chapman-Hall CRC Computational Science, 2012.

[36] Bradley Watanabe. *A Small Scale Reaction Wheel Prototype for Attittude Stabilization of Cubesats.* Master's, University of California Santa Cruz, 2013.

[37] E.W. Weisstein. "Legendre Polynomial." From MathWorld–A Wolfram Web Resource. http://mathworld.wolfram.com/LegendrePolynomial.html.

[38] Bong Wie. *Space Vehicle Dynamics And Control.* American Institute of Aeronautics and Astronautics, Reston, Virginia, 2 edition, 2008.

[39] Rafal Wisniewski and Piotr Kulczycki. Slew Maneuver Control for Spacecraft Equipped with Star Camera and Reaction Wheels. *Control Engineering Practice*, 13(3):349–356, 2005.